

Carbon Monoxide Production and Excitation in Comet C/1995 O1 (Hale-Bopp): Isolation of Native and Distributed CO Sources

Michael A. DiSanti

Department of Physics, The Catholic University of America, Washington, D.C. 20064 and Laboratory for Extraterrestrial Physics, NASA Goddard Space Flight Center, Code 690, Greenbelt, Maryland 20771
E-mail: disanti@kuiper.gsfc.nasa.gov

Michael J. Mumma

Laboratory for Extraterrestrial Physics, NASA Goddard Space Flight Center, Code 690, Greenbelt, Maryland 20771

Neil Dello Russo

Department of Physics, The Catholic University of America, Washington, D.C. 20064 and Laboratory for Extraterrestrial Physics, NASA Goddard Space Flight Center, Code 690, Greenbelt, Maryland 20771

and

Karen Magee-Sauer

Department of Chemistry and Physics, Rowan University, Glassboro, New Jersey 08028

Received September 28, 1999; revised May 21, 2001

The release of carbon monoxide from Comet C/1995 O1 Hale-Bopp was studied between June 1996 and September 1997 using high resolution infrared spectroscopy near 4.7 μm . The excitation of CO molecules in the coma was assessed through measurement of the rotational temperature on several dates at an angular resolution of ~ 1 arcsecond. An increase in T_{rot} with distance from the nucleus was revealed, most likely because of photolytic heating by fast H-atoms. Observed temperature profiles varied from date to date, but overall the degree of heating was most pronounced near perihelion. The similar rotational temperatures observed for CO and HCN may indicate control of rotational populations by collisions with electrons.

The spatial distribution of CO molecules in the coma revealed two distinct sources for CO, one being CO ice native to the nucleus, and another being CO released from a progenitor distributed in the coma. Only the native source was seen when the comet was beyond 2 AU from the Sun. Based on pre- and post-perihelion observations on five dates with heliocentric distance R_h between 4.10 and 2.02 AU, a heliocentric dependence $Q_{\text{CO,native}} = (1.06 \pm 0.44) \times 10^{30} R_h^{-1.76 \pm 0.26}$ molecules s^{-1} was obtained. Within $R_h \sim 1.5$ AU, however, both native and distributed sources were consistently present on all dates of observation. The total CO produced was the sum of the two sources and, based on seven dates, obeyed $Q_{\text{CO,total}} = (2.07 \pm 0.20) \times 10^{30} R_h^{-1.66 \pm 0.22}$ molecules s^{-1} . This heliocentric dependence was consistent with that found for water ($Q_{\text{H}_2\text{O}} \propto R_h^{-1.88 \pm 0.18}$ between 0.93 and 1.49 AU) and for mm-sized dust ($R_h^{-1.7 \pm 0.2}$ between 0.9 and 2.5 AU). Our derived total mixing ratio for CO was $Q_{\text{CO,total}}/Q_{\text{H}_2\text{O}} = 0.241 \pm 0.009$, with native and

distributed sources each contributing an abundance of approximately 12 percent that of water. This was the case even after correcting measured CO and H_2O column densities, and hence production rates, for opacity in the solar pump. The distributed source exhibited behavior consistent with thermal destruction of a precursor material. The observed variations in its production rate and spatial distribution along the slit suggested contributions from both a diffuse source in the coma and possibly from one or more jets enriched in CO or CO-containing material, such as CHON grains. © 2001 Academic Press

Key Words: comets; ices; infrared spectroscopy; carbon monoxide; extended emission.

INTRODUCTION

Carbon monoxide gas is ubiquitous in giant molecular clouds associated with regions of active star formation (Rank *et al.* 1971, Turner 1989); its high volatility makes it an excellent probe of conditions in cold shielded regions such as the natal clouds around young planetary systems (Chiar *et al.* 1995, Whittet *et al.* 1996). CO is found in both H_2O -rich (polar) and H_2O -poor (nonpolar) icy mantles on dust grains, depending on local conditions. In sufficiently cold quiescent regions surrounding the embedded star, carbon monoxide can condense directly, forming water-poor nonpolar ice. Closer to the star, CO is found as a minor component trapped in water-rich polar ice (Tielens *et al.* 1991, Chiar *et al.* 1995, Whittet *et al.* 1996, Chiar *et al.*

1998). Carbon monoxide was probably abundant in the cool outer regions of the presolar nebula where comets are thought to have formed, but the origin of CO in comets is uncertain and indeed may differ among comets depending on their distance of formation from the young sun.

Did the ice in Comet Hale-Bopp originate in the interstellar natal cloud, or did it form later by condensation from gas in the preplanetary disk? Interstellar nonpolar (CO-rich) ices could not have survived within about 40 AU of the proto-sun, but interstellar CO trapped in a polar ice could have survived in the giant-planets nebular region, at least until temperatures exceeded the sublimation point of water vapor (perhaps near 5 AU). Carbon monoxide could have condensed directly from nebular gas in the region beyond Neptune where temperatures were sufficiently low (<25 K). Closer to the young sun, higher temperatures would have prevented direct condensation. However, capture of CO from nebular gas could still proceed at temperatures as high as 50 K if it co-condensed with water (Sandford and Allamandola 1988), and there is evidence that some fraction of captured CO can remain trapped to much higher temperatures (e.g., ~ 150 K; Crovisier and Encrenaz 2000). Thus, the amount of native CO retained in the cometary nucleus (and its abundance relative to water ice) provides an important clue to the origin of this material and to conditions in the precometary environment (Mumma *et al.* 1993).

The discovery of cometary CO during rocket ultraviolet observations of Comet West (1976 VI) revealed a substantial abundance (20–25%) relative to H₂O (Feldman and Brune 1976, Feldman 1978), and established this molecule as an important component in these primitive solar system objects. Yet subsequent observations of more than three dozen comets, particularly with the International Ultraviolet Explorer (IUE) (Festou and Feldman 1987, Festou 1990), yielded CO detections in only a few. When detected, the derived CO abundance appeared to vary considerably from comet to comet; e.g., IUE observations of Comet Bradfield (1979 X) yielded CO/H₂O $\sim 2\%$, or about one-tenth that observed for West (A'Hearn and Feldman 1980). It was suggested that these differences could be related to the aperture sizes of the rocket-UV and IUE observations, which differed greatly.

Although present as a native ice in the nucleus, carbon monoxide can also be produced in the cometary coma from other precursors, where it can then exhibit both direct and extended (or distributed) sources in comets. In-situ Giotto spacecraft observations of Comet 1P/Halley (1986 III) revealed that only one-third ($\sim 3.5\%$ relative to water) of the total CO was released directly from the nucleus, the remainder ($\sim 7.5\%$) being produced from a source distributed in the coma (Eberhardt 1999, Eberhardt *et al.* 1987). This discovery sparked keen interest in identifying the key mechanism(s) responsible for production of the distributed CO source. An alternative view in which Giotto flew through a jet enriched in CO was proposed by Greenberg and Li (1998).

Photolysis of monomeric formaldehyde (H₂CO) was suggested as a significant (though apparently insufficient) source for distributed CO (Meier *et al.* 1993) based on the H₂CO abun-

dance as inferred from Giotto Neutral Mass Spectrometer observations (Krankowsky 1990). Giotto also discovered organic (CHON) particles (Kissel *et al.* 1986) which, coupled with evidence for a dominant distributed source of H₂CO (perhaps even the sole formaldehyde source) in Halley (Snyder *et al.* 1989, Krankowski 1990, Meier *et al.* 1993, Eberhardt 1999), led to scenarios whereby H₂CO, released from outflowing CHON particles, could contribute additional CO. Proposed mechanisms involved release of polymerized formaldehyde (Meier *et al.* 1993), or possibly polyoxymethylene (POM) (Mitchell *et al.* 1987, Huebner 1987, Huebner *et al.* 1987, Mitchell *et al.* 1989, Eberhardt 1999), to account for the observed distributions of H₂CO and CO. An additional proposed contributor was carbon suboxide (C₃O₂) (Huntress *et al.* 1991), suggested to supply not only CO, but also to account for the abundance and distribution of neutral carbon atoms as inferred from Giotto observations of the CO⁺ ion in Halley (Balsiger *et al.* 1986).¹ However, Crovisier *et al.* (1991), using the VEGA 1 IKS spectrum of Halley (Combes *et al.* 1988), argued that C₃O₂ could be at most a minor contributor. They derived an upper limit C₃O₂/H₂O $\sim 10^{-3}$, well below the minimum value (0.03–0.04) required to produce the amount of distributed CO inferred from the Giotto observations.

The first ground-based detection of cometary CO at infrared wavelengths was in Comet Austin (1989c1), through tentatively identified emission in the P(3) line of the $v = 1 - 0$ fundamental band near $4.7 \mu\text{m}$ (DiSanti *et al.* 1992). A comparison of measured line intensities contained within 2×3 -arcsecond and 2×9 arcsecond apertures was consistent with a purely native CO source. However, the low signal-to-noise ratio (~ 5) and non-detection of P(2) emission, whose strength should have been comparable to that of P(3), precluded further conclusions as to the origin of CO in this comet.

The first definitive ground-based IR detection of cometary CO was in Comet C/1996 B2 (Hyakutake) (Mumma *et al.* 1996). Studies using different sized apertures suggested the presence of both native and distributed CO sources. Small apertures on ground-based (at IR wavelengths; Mumma *et al.* 1996) and space-based (at UV wavelengths; Feldman *et al.* 1996, Weaver *et al.* 1996) platforms provided abundances of 5–10%, well below the values (20–30%) derived from large-beam observations (in the radio; Womack *et al.* 1997a, Biver *et al.* 1999a). The small-beam studies sampled primarily native CO (and may be influenced by optical depth effects), while larger fields of view included both native and distributed CO sources. The abundance of CO ice in the nucleus can be obtained only after discriminating

¹ Recent studies of HNC/HCN (Biver *et al.* 1997, Irvine *et al.* 1998, 1999), and of HCO⁺ (Lovell *et al.* 1998) in the coma of Comet Hale-Bopp, suggest a potentially important role for chemistry in the coma, involving supra-thermal hydrogen atoms and/or ion-molecule reactions (Rodgers and Charnley 1998). However, these processes are expected to be important primarily for trace species. By contrast, the production of CO from distributed sources rivals that from the native source (CO-ice) in Hale-Bopp, and is a major contributor of volatile carbon (see text).

the native and distributed sources, and until now this had not been accomplished by remote observations.

The apparition of the bright long period comet C/1995 O1 (Hale-Bopp), coupled with major technological advances

TABLE I
Log of Hale-Bopp Co Observations

UT Date	R_h^a	Δ^a	$\Delta\text{-dot}^b$	PA ^c	β^d	Lines Observed	t_{int}^e	Mid-UT ^f
1996								
13 Jun	4.10	3.17	-30.9	246	07	P1, P2	2960	13.57
19 Sep	3.03	2.92	+09.1	92	19	P2, P3	280	19.23
11 Dec	2.02	2.83	-18.0	31	13	P2, P3	360	11.01
						R2, R3	240	11.06
1997								
21 Jan	1.49	2.20	-32.5	335	22	P2, P3	240	21.75
						P1, P2	240	21.80
						R0, R1	240	21.80
						R2, R3	240	21.81
						R4, R5	240	21.82
24 Feb	1.11	1.57	-28.8	327	39	R5, R6	120	21.83
						R2, R3	120	24.00
						R5, R6	120	24.00
						R7, R8	120	24.01
01 Mar	1.06	1.47	-24.8	330	42	R2, R3	120	01.85
						R0, R1	120	01.86
						R5, R6	120	01.87
						R7, R8	120	01.88
09 Apr	0.93	1.44	+21.8	43	44	P1, P2	120	01.89
						P2, P3	60	09.88
						R0, R1	120	09.90
						R2, R3	60	09.90
						R5, R6	60	09.91
16 Apr	0.95	1.53	+25.7	54	40	P2	120	09.92
						R9, R10	60	09.93
						R0, R1	120	16.04
						R5, R6	120	16.06
						R9, R10	120	16.08
30 Apr	1.05	1.75	+29.6	75	31	P2	120	16.09
						R9, R10	120	30.09
						R0, R1	60	30.15
						R5, R6	120	30.15
01 May	1.06	1.77	+29.7	76	30	R0, R1	60	01.01
						R5, R6	60	01.07
						R9, R10	120	01.14
						R2, R3	120	01.17
08 Aug	2.25	2.91	+08.9	221	17	R0, R1	300	08.82
						P2, P3	420	08.84
						R2, R3	720	08.89
25 Sep	2.83	3.09	+06.1	253	19	R0, R1	1320	25.70

^a Heliocentric and geocentric distances in AU.

^b Geocentric Doppler shift (km s⁻¹).

^c Position angle (degrees) of the anti-solar direction (i.e., the extended heliocentric radius vector), projected onto the sky plane and measured eastward from north.

^d Phase angle (degrees) of the comet (i.e., the angle Sun-Comet-Earth). On all dates spanning our Hale-Bopp observations, β was highly acute, thus the anti-solar direction as largely away from the observer (the extended heliocentric radius vector makes the angle 180°- β with the Earth-Comet direction; see Fig. 1).

^e Total integration time on source (s).

^f Mid-exposure UT (decimal date).

(construction of large sub-mm telescopes, and implementation of spectrometers with sensitive infrared array detectors), permitted studies of the evolution of cometary activity in unprecedented detail. Observations from heliocentric distances (R_h) ~4–7 AU indicated CO-driven sublimation (Biver *et al.* 1996, Jewitt *et al.* 1996, Biver *et al.* 1997, Womack *et al.* 1997b). Activity at large distances had been seen previously in some comets, most notably Halley, Schwassmann-Wachmann 1 (S-W 1), and 2060 Chiron (Huebner *et al.* 1992). For S-W 1 (Senay and Jewitt 1994, Crovisier *et al.* 1995) and 2060 Chiron (Womack *et al.* 1999), the derived CO production rate was sufficient to account for the observed coma. For Hale-Bopp, CO production at large distances rivaled or exceeded that exhibited by weaker comets near perihelion, and this held promise for high levels of activity as Hale-Bopp entered the inner solar system.

Here we report results from an extended study at infrared wavelengths of the evolution of carbon monoxide production in Comet Hale-Bopp. Our serial spectral-spatial observations (Table I) span a large range in time and in heliocentric distance, from June 1996 ($R_h = 4.10$ AU preperihelion) to September 1997 ($R_h = 2.83$ AU postperihelion). Our study discriminates native and distributed contributions to the total CO production and reveals the onset of the distributed source between $R_h \sim 2.0$ and 1.5 AU preperihelion. Aspects of this work were reported elsewhere (DiSanti *et al.* 1999) but are here expanded upon and augmented. We present our data base of CO observations having the nucleus contained within the slit, and discuss coma properties derived from these observations. A detailed discussion of the excitation of CO molecules in the coma as a function of line-of-sight distance from the nucleus is also presented, as is discussion of possible scenarios for release of the distributed CO component.

OBSERVATIONS AND DATA REDUCTION

We used the cryogenic echelle grating spectrometer (CSHELL) on the NASA IRTF 3-meter telescope at Mauna Kea Observatory, Hawaii. CSHELL incorporates a 256 × 256-pixel InSb array detector, with sensitivity in the 1–5.5 μm spectral region (Tokunaga *et al.* 1990, Greene *et al.* 1993). The small pixel size (0.2 arcsecond) provides seeing-limited angular resolution along the 30 arcsecond-long slit, which we oriented east-west. The single-pixel spectral resolving power ($\nu/\Delta\nu$) for CSHELL is $\sim 10^5$ (3 km s⁻¹ pixel⁻¹). Thus, a source which uniformly fills the 1 arcsecond slit (e.g., a sky emission line) employed for the comet observations will have $\nu/\Delta\nu \sim 2 \times 10^4$. For a point source (star) with optimal focus and perfect telescope tracking, the resolving power is determined by the point-spread-function, which is largely a function of the seeing at the time of observation. This can be sub-arcsecond at times, resulting in $\nu/\Delta\nu$ approaching 3×10^4 . For most of our Hale-Bopp observations, $\nu/\Delta\nu = 2.0 - 2.5 \times 10^4$, sufficient to isolate line emission in the CO $v = 1 - 0$ ro-vibrational band from the adjacent corresponding absorption features in the terrestrial atmosphere, and from underlying cometary continuum emission.

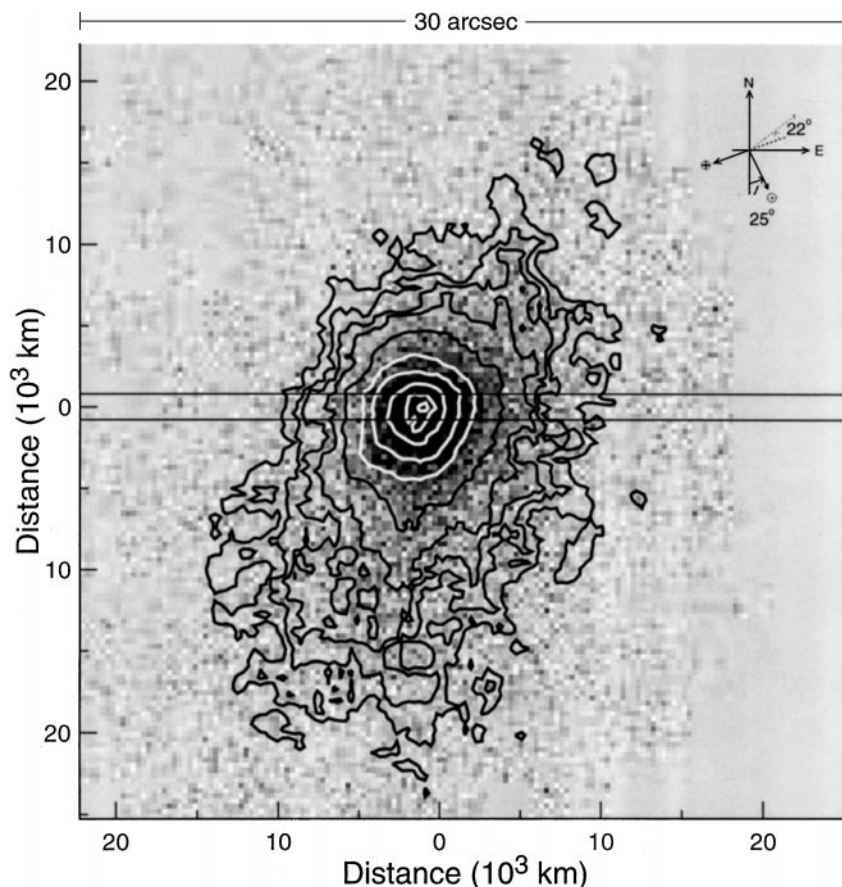


FIG. 1. Gray-scale image (2 s exposure time) of Comet Hale-Bopp, obtained on 1997 January 21 through the CVF, showing the morphology of the dust coma near $2.2 \mu\text{m}$ (4500 cm^{-1}), with black corresponding to higher intensity. The $1'' \times 30''$ slit is shown running horizontally (east–west) and centered on the nucleus. The white contours correspond to 417, 398, 355, 282, and 224 counts, and the black contours correspond to 141, 89.1, 66.8, 50.1, and 31.6 counts; 1 count corresponds to a flux density of approximately $3 \times 10^{-21} \text{ watt m}^{-2}/\text{cm}^{-1}$. The total flux density contained within a $1'' \times 1''$ ($\sim 1,600 \times 1600 \text{ km}$) aperture centered on the nucleus is $\sim 3 \times 10^{-17} \text{ watt m}^{-2}/\text{cm}^{-1}$. The phase angle $\beta = 22^\circ$ shown in the directional inset indicates that the anti-sunward direction points away from the observer, making an angle of 68° with the plane of the sky. Thus, the sunward direction is out of the sky at this angle, and lies 25° east of south.

We used an observing sequence ABBA, where A represents observations with the comet centered in the slit, while for B scans the telescope was nodded 2 arc-minutes perpendicular to the slit length (north or south) to sample sky emission.² The net comet signal was isolated as $A - B - B + A$. Flat field (continuum lamp) spectra and dark frames were obtained immediately after each ABBA set, and the comet was frequently imaged through the CVF (Fig. 1).³ Processing of our spectroscopic observations begins with flat-fielding, removal of “hot” pixels, and straightening of frames (i.e., pixel resampling) for consistent spatial–spectral registration (see Fig. 2, and Dello Russo

et al. 1998 for details). The result for each sequence is a spatial–spectral frame, in which the spectral dimension falls along rows, and the spatial dimension falls along columns (Fig. 2D).

To establish the wavelength calibration for our CSHELL spectra, we use the Spectrum Synthesis Program (Kunde and Maguire 1974), which accesses the HITRAN-1992 Molecular Database (Rothman *et al.* 1992). We compare the atmospheric emission lines contained in our sky (i.e., B-frame) observations (Figs. 2E and F) with a calculated sky radiance spectrum. This process results in row-by-row spectral registration, which is applied to comet and sky frames (compare Fig. 2C with Fig. 2D, and Fig. 2E with 2F). We next apply this calibration solution to a one-dimensional spectral extract of the comet (Fig. 2G, top trace), which contains cometary continuum and superimposed line emissions. Through comparison with a calculated transmittance spectrum, the terrestrial atmospheric absorption lines in the comet spectrum establish the absolute column burden for each absorbing species in the terrestrial atmosphere, and also allow us to correct for small frequency shifts (relative to the corresponding sky line positions) that occur when the

² Based on test observations, no cometary CO emission was present in the “sky” beam, at the noise level of the data.

³ Virtually all of our Comet Hale-Bopp observations were conducted during daylight, hence the CCD autoguider for CSHELL was not available for use. We therefore obtained images of the comet near 2.2 or $3.5 \mu\text{m}$ immediately following each ABBA/flat/dark sequence, to check for cometary drift (which was generally < 1 arcsecond), and to update telescope tracking rates as needed. The interval between images was typically 6–8 minutes, and discernable drift perpendicular to or along the slit was taken into account in the ensuing analysis.

comet is not quite centered in the slit. The atmospheric transmittance spectrum is calculated at monochromatic resolution for the optimized atmospheric model, and is then binned to the instrumental sampling interval, convolved to the spectral resolution of the comet data, and scaled to the cometary continuum.

Subtraction of this optimized synthetic continuum from the observed comet spectrum isolates the cometary molecular emissions (the “residuals” in Fig. 2G). These are still convolved with the atmospheric transmittance function. The true line intensity incident at the top of the terrestrial atmosphere is obtained by ratioing the measured intensity to the fully resolved transmittance at the Doppler-shifted line-center frequency. Absolute flux calibration (watts m⁻²) is achieved by comparison with spectra of flux-standard stars obtained through a 4 arcsecond-wide slit.

Observing CO in the $v = 1 - 0$ fundamental band from the ground requires a radial velocity of the comet relative to the earth. Examples of extracted CO spectra are presented for several dates in Figs. 3A (preperihelion) and 3B (postperihelion). For each spectrum, observed frequencies and flux densities are indicated. Each cometary emission line is Doppler-shifted from its rest frequency according to the geocentric velocity of Comet Hale-Bopp (Δ -dot, Table I), and corrections for atmospheric transmittance have not yet been applied. Thus, apparent intensities of spectral lines, even those within the same spectrum, are in general not representative of the true cometary emission intensities. Care must also be exercised when comparing continuum flux densities taken from different spectra, as these are influenced by seeing effects and by telescope tracking over the course of each exposure.

A frame showing cometary line emission alone is obtained by subtracting the modeled dust continuum (row-by-row) from the straightened spatial-spectral frame containing both emissions (Figs. 2D, 4A). This procedure isolates emission from cometary volatiles (CO and H₂O in the frame shown). The spatial distribution along slit (spatial profile) of CO emission is obtained for each line by summing the signal over five adjacent columns (spectral channels), centered on the column corresponding most closely to the Doppler-shifted line-center frequency.⁴ This is a measure of the distribution along the slit of CO molecules in the upper state of the transition giving rise to the line in question (Fig. 4B). (For the P1 and P2 lines, these are rotational levels $J' = 0$ and $J' = 1$, respectively, of the first excited vibrational state, $v' = 1$.) Spatial profiles are similarly obtained for other volatiles (e.g., H₂O; Fig. 4C). The spatial distribution of dust emission (dashed line, Figs. 4B, 4C) is obtained by sampling columns not containing cometary emission lines. On this date, CO emission is spatially more extended than either the water or continuum emission. The spatial distributions of water and dust are similar and are slightly asymmetric toward the east, while CO is markedly more extended toward the east than either water or dust (Fig. 4C).

⁴ For the 1 arcsecond-wide slit, five columns corresponds to the approximate FWHM of each CO line. A small correction factor (~ 1.15) was applied to account for signal not included in the 5-column sum.

MAPPING OF CO EXCITATION

At a given position along the slit, the CO rotational temperature (T_{rot}) is determined from intensities measured for several CO lines (after correcting for atmospheric transmittance). For simple linear molecules, the emission intensity of a ro-vibrational line is given by (Herzberg 1950),

$$I_{\text{em}} = (C'_{\text{em}}/Z_r)v^4(J' + J'' + 1)\exp[-B'J'(J' + 1)x/T_{\text{rot}}], \quad (1a)$$

where ν is the line frequency (cm⁻¹), and $x \equiv hc/k \approx 1.44$ cm K (h is Planck’s constant, and k is Boltzmann’s constant). The quantum numbers J' and J'' refer to the upper and lower rotational states, respectively, of the transition, and B' is the rotational constant of the upper vibrational state ($v \equiv v' = 1$). The factor C'_{em} is a constant which depends on the change of dipole moment associated with the transition and on the number of molecules in $v' = 1$, and Z_r is the rotational partition function for the molecule at temperature T_{rot} . We recast Eq. (1a) in terms of our (transmittance-corrected) line flux, F_{line} (watts m⁻²), as

$$F_{\text{line}} = (C_{\text{em}}/Z_r)N_{1,J'}v^4(J' + J'' + 1)\exp[-B'J'(J' + 1)x/T_{\text{rot}}], \quad (1b)$$

where the constant C_{em} now incorporates geometrical considerations and the change in dipole moment,⁵ and we explicitly

⁵ The column brightness (watts m⁻² sr⁻¹) for emitted line radiation is given by

$$I_{\text{em}} = (1/4\pi)N_{1,J'}hc\nu A_{J',J''},$$

where $N_{1,J'}$ is the column density (molecules m⁻²) in the upper state of the transition ($v' = 1, J'$), and $A_{J',J''} = (64\pi^4/3h)v^3|R_{\text{em}}|^2$ is the Einstein transition probability (s⁻¹) for ro-vibrational emission from initial state ($1, J'$) to final state ($0, J''$). The moment R_{em} represents the matrix element of the electric dipole corresponding to the transition between ($1, J'$) and ($0, J''$) states. The term $|R_{\text{em}}|^2 = S_J|\mu|^2$, where the “line strength” $S_J = (1/2)(J' + J'' + 1)/(2J' + 1)$ isolates the J-dependence of R_{em} , and $\mu = 1.12 \times 10^{-19}$ esu-cm is the (permanent) electric dipole moment for the CO molecule (Lang 1980). [$S_J = J'/(2J' + 1)$ for R-branch lines ($J'' = J' - 1$), and $S_J = (J' + 1)/(2J' + 1)$ for P-branch lines ($J'' = J' + 1$).] The rotational population in $v' = 1$ is characterized by a single temperature (cf. Fig. 5), hence,

$$N_{1,J'} = N_1\{(2J' + 1)\exp[-B'J'(J' + 1)x/T_{\text{rot}}]\}/Z_r.$$

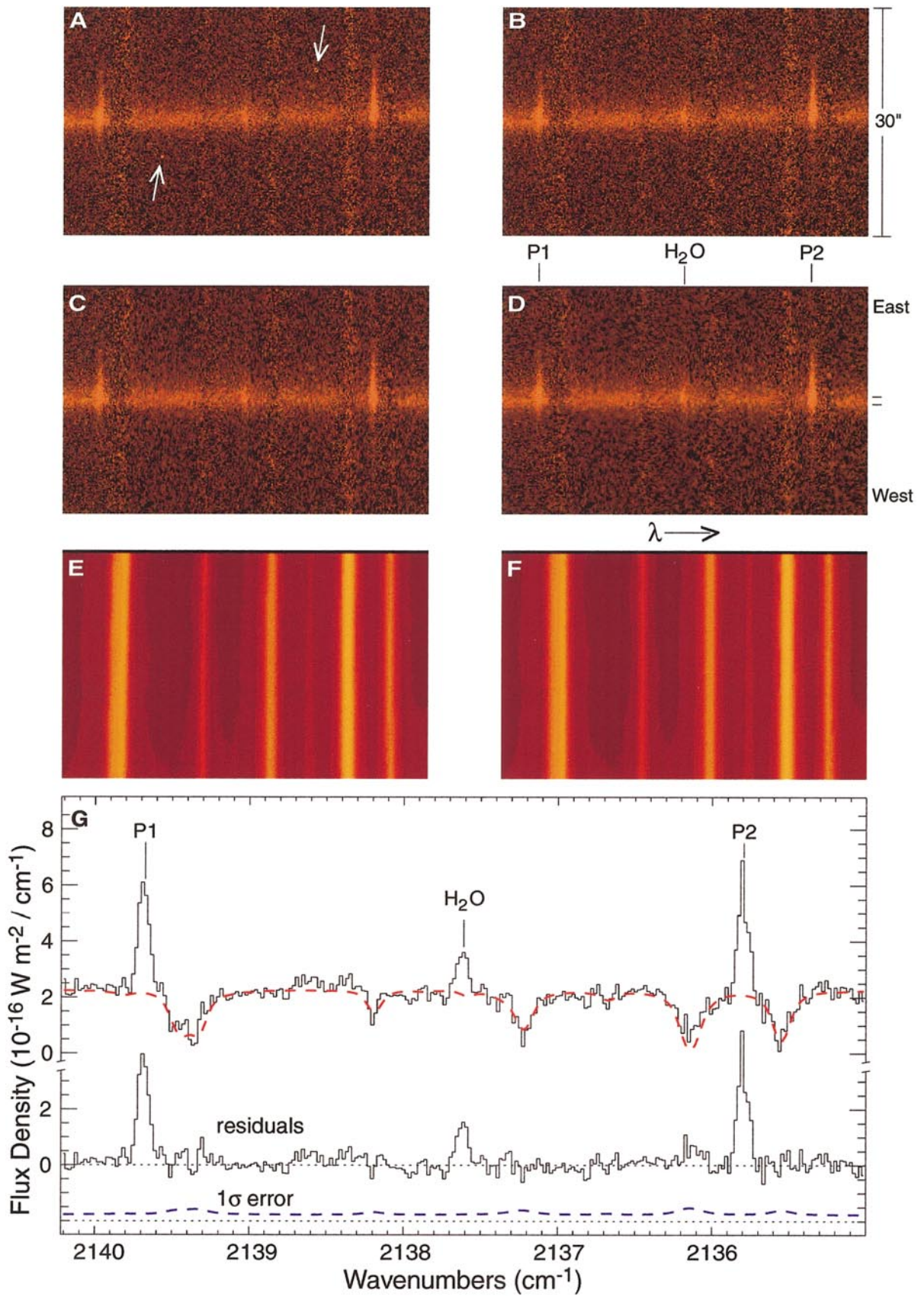
The line flux (watts m⁻²) incident at the telescope aperture from solid angle Ω is then

$$\begin{aligned} F_{\text{line}} &\equiv \Omega I_{\text{em}} = (\Omega/4\pi)(64\pi^4/3h)v^3|R_{\text{em}}|^2hc\nu N_1\{(2J' + 1) \\ &\quad \times \exp[-B'J'(J' + 1)x/T_{\text{rot}}]\}/Z_r \\ &= (8\pi^3c\Omega/3)|\mu|^2v^4N_1\{(J' + J'' + 1)\exp[-B'J'(J' + 1)x/T_{\text{rot}}]\}/Z_r. \end{aligned}$$

For our $1'' \times 1''$ stepped aperture (cf Eq. 2 and accompanying discussion), $\Omega = \Omega_1 = 2.35 \times 10^{-11}$ sr. Comparing this last expression for F_{line} with Eq. (1b) leads to

$$C_{\text{em}} = (8\pi^3c\Omega_1/3)|\mu|^2 \cong 7.31 \times 10^{-40} \text{ watt cm}^4.$$

Equation (1b) can be used to predict values for N_1 as a function of line-of-sight through the coma, and this provides clues to line-by-line opacity effects in the inner coma (see Appendix).



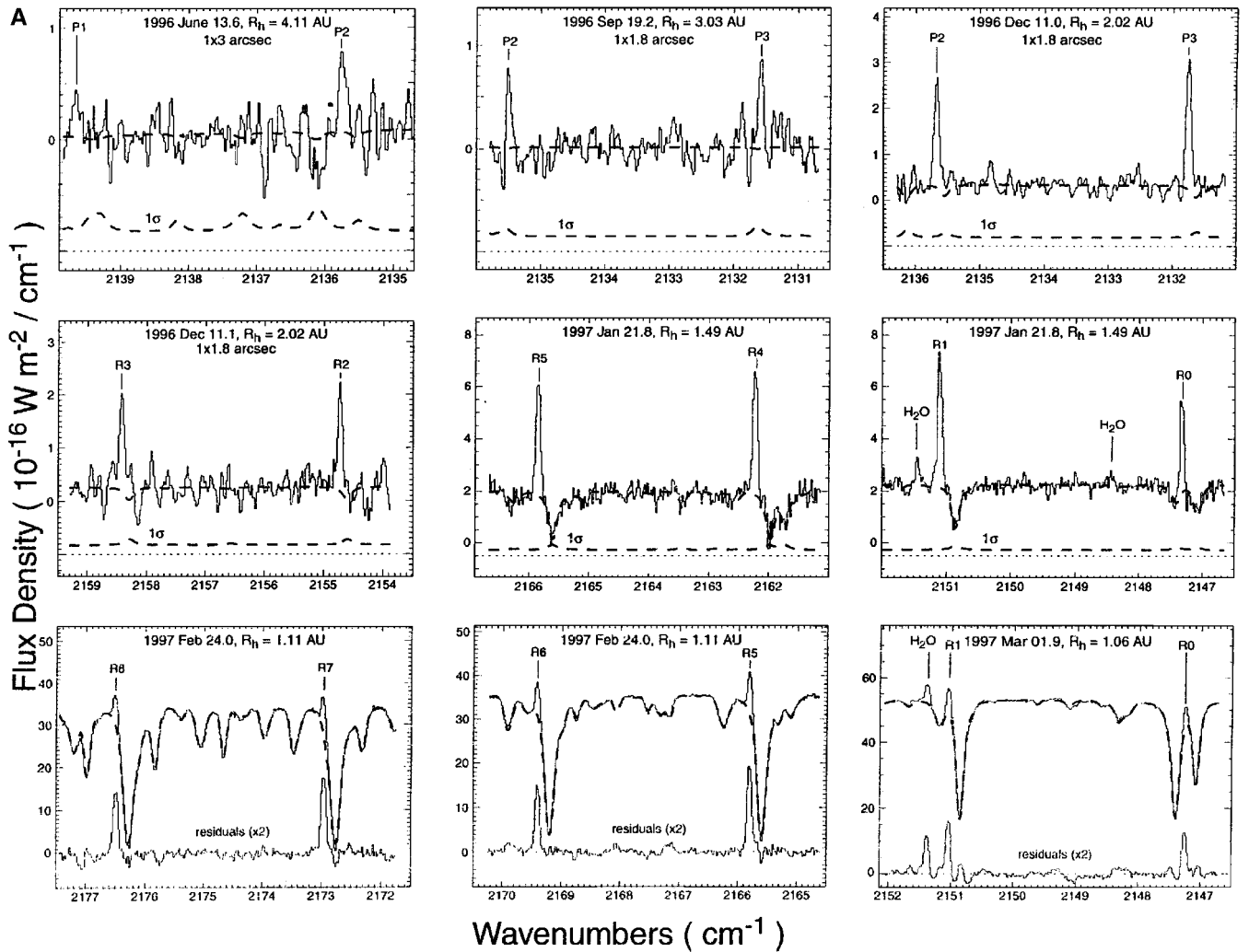


FIG. 3. Overview of CO emission in Comet Hale-Bopp, obtained with CSHELL through the 1-arcsecond-wide slit. A. Representative preperihelion spectra. For all but the first spectrum shown, the spectral resolving power $\nu/\Delta\nu \sim 25,000$. The June 1996 spectrum was binned by 2 in the spectral dimension to improve the signal-to-noise ratio, thus $\nu/\Delta\nu \sim 12,000\text{--}14,000$ for it. All extracts were centered on the row containing the peak continuum emission and, unless otherwise noted, represent sums over 1 arcsecond along the slit (5 rows). For the panels in which the 1σ stochastic error is shown (offset as in Fig. 2G), this error dominates the uncertainty. Residual emissions are shown for dates when the cometary continuum was extremely bright. For those spectra, the overall uncertainty (scatter) is dominated by other effects such as slight residual instrumental fringing, small errors in the frequencies of modeled (SSP) atmospheric absorption lines, etc. Analysis of indicated cometary water emissions has been included in a separate publication (Dello Russo *et al.* 2000). Corrections for atmospheric transmittance have not yet been applied, thus the apparent line intensities are generally not representative of their true cometary emission intensities. B. Representative postperihelion spectra.

FIG. 2. Sequence of steps illustrating the initial processing of two-dimensional (spatial-spectral) frames of CSHELL data. In this example from UT 1997 January 21.8, Comet Hale-Bopp was observed through a 1-arcsecond-wide slit, yielding a spectral resolving power $\nu/\Delta\nu \sim 2.5 \times 10^4$. The slit length (indicated on the right) is 30 arcseconds ($\sim 4.8 \times 10^4$ km at the comet). Frames A–D show the net (sky-subtracted) comet signal, with wavelength increasing to the right. The cometary continuum extends left–right across each frame, and superimposed on it are two emission lines of the CO $v = 1 - 0$ fundamental band, and one line ($0_{00} - 1_{01}$) of the water $\nu_3 - \nu_2$ hot band (Dello Russo *et al.* 2000). A. Flat-fielded difference frame (comet–sky–sky+comet). Deviant pixels can be seen as light-colored specks (indicated by white arrows), and the continuum tilts upward from left to right. B. Difference frame following pixel cleaning, but prior to straightening. C. Difference frame straightened along rows, so that all pixels along a given row correspond to a common spatial position along the slit (note the now-horizontal continuum). D. Difference frame straightened along columns, so that all pixels along a given column correspond to a common mean frequency. E. Corresponding sky frame prior to applying the column-straightening step. The sky emission lines are clearly tilted from vertical, and the spectral dispersion ($\text{cm}^{-1}/\text{column}$) varies from row to row. F. Sky frame after column-straightening. G. Spectral extract, representing the signal summed over five rows centered on the peak continuum intensity (vertical extent indicated to the right of Fig. 2D). Subtraction of the atmospheric model (superimposed dashed curve) yields the residual cometary molecular emissions in excess of the continuum. The bottom dashed curve represents the 1-sigma stochastic error, and its zero level is indicated by the lower dotted line.

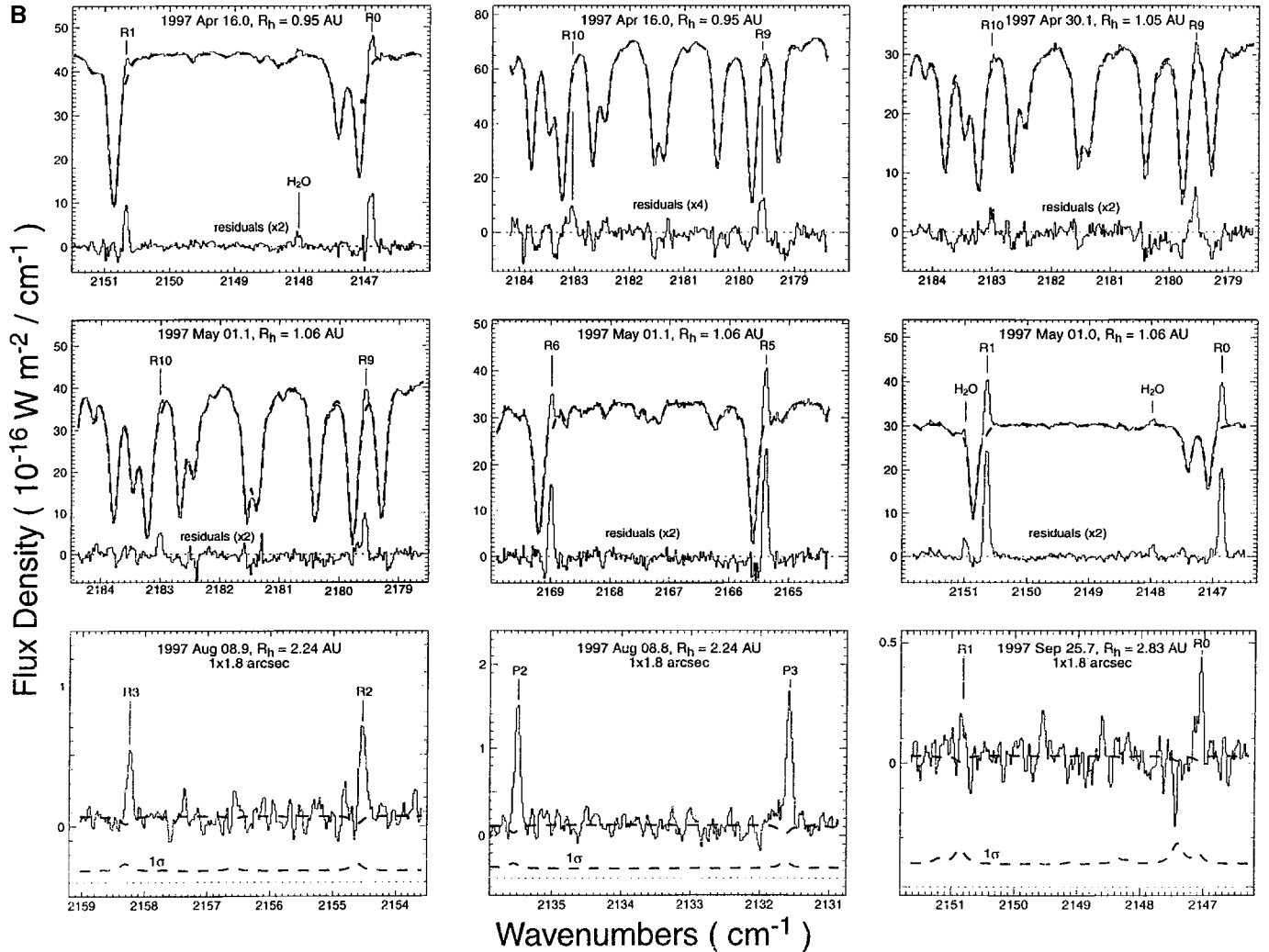


FIG. 3—Continued

show the dependence upon the column density N_1 (molecules m^{-2}) in $v' = 1$.

Rotational temperatures for CO were retrieved on all dates of observation between 0.93 and 2.24 AU of the Sun (See Fig. 5 and Table II). The effective rotational temperature for the $v' = 1$ state is determined by comparing $(k/hcB') \ln[F_{\text{line}}/v^4(J' + J'' + 1)]$ against $J'(J' + 1)$ for the lines observed. A linear least squares fit has slope $-1/T_{\text{rot}}$. In Fig. 5 (left panels), we show for each date the derived temperature, based on measured line intensities over the range of cometocentric distances used to determine our CO production rates (see discussion below, and caption to Fig. 5). For CO, we take $B' = B'' = 1.97 \text{ cm}^{-1}$ (Herzberg 1950). (Because infrared radiative pumping and decay control the population in $v' = 1$, and many rotational levels are populated, the rotational temperatures in $v' = 1$ and $v'' = 0$ should be very nearly the same; see Chin and Weaver 1984 and Magee-Sauer *et al.* 1999 for further discussion.)

For each date, we measured the rotational temperature at 1-arcsecond intervals along the slit (Fig. 5, right panels). For dates

near 1 AU from the Sun (e.g., Figs. 5D–5H), we observed an increase in T_{rot} when moving away from the nucleus. (The profile of retrieved temperature versus line-of-sight distance (ρ) from the nucleus is not strictly identical to the radial temperature profile. The distance ρ represents the “impact parameter” for the beam; i.e., the *minimum* distance from the nucleus along a given line-of-sight, and T_{rot} measures the mean rotational temperature for molecules in the beam.) Our CO data do not support more than one rotational temperature (e.g., one for low- J lines and another for high- J lines) along any line-of-sight, although this assessment may be complicated by differing optical depths between different CO lines for beam positions passing close to the nucleus.

Under optically thin conditions, the relative intensities of P- and R-branch lines originating from a common upper state ($v' = 1, J'$) are given by the statistical branching ratio $(J' + 1)/J'$. With increasing optical depth (e.g., in the inner coma), a net transfer of energy from the P-branch line to the R-branch line results, and this is most noticeable when the lower state

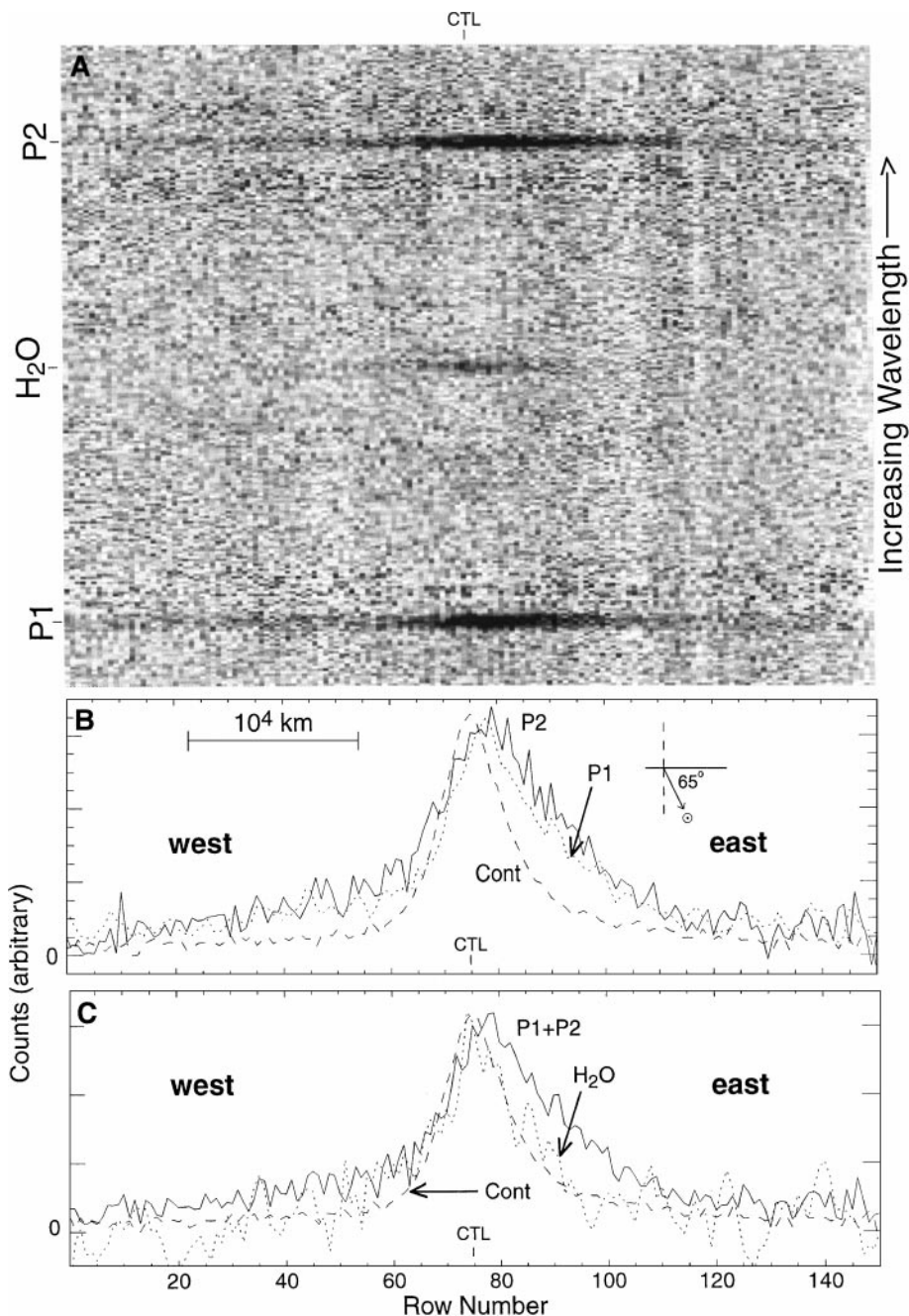


FIG. 4. A. Processed spatial-spectral image of Hale-Bopp obtained on UT 1997 January 21, following row-by-row scaled subtraction of the modeled cometary continuum. Note the considerably greater spatial extent of the CO P1 and P2 emission lines compared with that of the H₂O line. The label “CTL” (centerline) denotes the row containing the peak continuum emission. B. Comparison of spatial profiles for CO lines and the continuum. The compass inset shows that the sunward direction lies 65° south of east; hence the sunward-facing hemisphere (projection along the slit) is toward the east. (We also adopt this convention for the insets in Figs. 5 and 6.) C. Comparison of summed P1 and P2 profiles with those of the continuum and H₂O. While the water profile closely follows the continuum, the CO emission is more extended and its peak is displaced to the east.

populations differ greatly, as for small values of J' (e.g., P2/R0, and P3/R1). This is seen in our excitation analysis as a reduced intensity for P2 and P3 compared with R0 and R1 for beam positions passing close to the nucleus (see Fig. A1). However, so long as collisional relaxation (of the upper state) is negligi-

ble, no quanta are lost and the mean Q derived for a given J' is unaffected (see Appendix for further discussion).

We observed similar rotational temperatures, and also an increase in T_{rot} with ρ , for HCN in Comet Hale-Bopp (Magesauer *et al.* 1999). Given the large difference in dipole moment

TABLE II
CO Rotational Temperatures in C/1995 O1 Hale-Bopp

UT Date ^a	ρ -range ^b	T _{rot} (east) ^c	T _{rot} (west) ^c	T _{rot} (mean) ^c
<i>1996</i>				
Dec 11.01–11.06	1.5–11.5 (3090–23690)	43 ± 15	78 ± 19	55 ± 9
<i>1997</i>				
Jan 21.74–21.83	0–1.5 (0–2380)	92 ± 4	103 ± 7	94 ± 5
	1.5–3.5 (2380–5550)	87 ± 3	82 ± 15	85 ± 5
	3.5–5.5 (5550–8730)	100 ± 14	81 ± 9	95 ± 9
	5.5–8.5 (8730–13500)	106 ± 8	92 ± 9	98 ± 6
	8.5–11.5 (13500–18250)	94 ± 15	85 ± 6	88 ± 6
Feb 23.99–24.01	3.5–11.5 (5550–18250)	101 ± 6	85 ± 4	95 ± 4
	0–1.5 (0–1710)	119 ± 6	115 ± 6	116 ± 4
	1.5–3.5 (1710–4000)	120 ± 3	129 ± 5	123 ± 3
	3.5–5.5 (4000–6290)	116 ± 10	147 ± 9	118 ± 7
	5.5–8.5 (6290–9720)	124 ± 4	129 ± 4	126 ± 3
Mar 01.85–01.89	8.5–11.5 (9720–13140)	122 ± 3	127 ± 6	124 ± 3
	3.5–11.5 (4000–13140)	119 ± 3	131 ± 4	122 ± 3
	0–1.5 (0–1600)	93 ± 5	93 ± 4	92 ± 3
	1.5–3.5 (1660–3750)	89 ± 2	97 ± 3	92 ± 3
	3.5–5.5 (3750–5890)	90 ± 2	106 ± 2	100 ± 5
Apr 09.88–09.93	5.5–8.5 (5890–9100)	95 ± 5	107 ± 2	102 ± 3
	8.5–12.5 (9100–13380)	96 ± 6	122 ± 6	111 ± 6
	5.5–12.5 (5890–13380)	96 ± 3	114 ± 4	106 ± 4
	0–1.5 (0–1570)	84 ± 7	69 ± 8	72 ± 6
	1.5–3.5 (1570–3670)	96 ± 3	74 ± 5	82 ± 6
Apr 16.04–16.09	3.5–5.5 (3670–5770)	101 ± 3	96 ± 4	98 ± 2
	5.5–8.5 (5770–8910)	105 ± 6	106 ± 5	105 ± 3
	8.5–12.5 (8910–13100)	116 ± 3	112 ± 2	114 ± 2
	5.5–12.5 (5770–13100)	110 ± 3	109 ± 3	110 ± 3
	0–1.5 (0–1670)	89 ± 10	109 ± 5	99 ± 7
Apr 30.09–30.15	1.5–3.5 (1670–3900)	87 ± 8	102 ± 5	92 ± 6
	3.5–5.5 (3900–6130)	112 ± 6	110 ± 4	110 ± 4
	5.5–8.5 (6130–9470)	108 ± 7	119 ± 3	118 ± 4
	8.5–12.5 (9470–13920)	112 ± 5	132 ± 4	125 ± 4
	5.5–12.5 (6130–13920)	114 ± 4	125 ± 3	122 ± 3
May 01.01–01.17	0–1.5 (0–1910)	82 ± 3	79 ± 2	81 ± 2
	1.5–3.5 (1910–4460)	88 ± 3	83 ± 7	86 ± 4
	3.5–5.5 (4460–7010)	99 ± 2	98 ± 4	99 ± 2
	5.5–8.5 (7010–10800)	114 ± 5	113 ± 12	113 ± 6
	8.5–11.5 (10800–14650)	116 ± 4	125 ± 8	119 ± 4
Aug 08.80–08.91	3.5–11.5 (4460–14650)	101 ± 2	104 ± 3	102 ± 2
	0–1.5 (0–1930)	67 ± 12	91 ± 24	81 ± 13 ^d
	1.5–3.5 (1930–4510)	91 ± 10	121 ± 9	112 ± 9
	3.5–5.5 (4510–7090)	77 ± 11	103 ± 6	94 ± 8
	5.5–8.5 (7090–11000)	76 ± 9	97 ± 5	92 ± 5
Aug 08.80–08.91	8.5–11.5 (11000–14820)	86 ± 7	118 ± 7	106 ± 7
	3.5–11.5 (4510–14820)	90 ± 5	107 ± 4	100 ± 4
	3.5–10.5 (7390–22170)	52 ± 18	62 ± 22	54 ± 12

^a Time interval over which CO observations included in the present analysis were obtained, in decimal UT date.

^b Range of projected distances ρ (in arcseconds, with km in parentheses) from the nucleus over which T_{rot} was determined.

^c Derived Co rotational temperatures as functions of ρ , measured east of the nucleus, west of the nucleus, and their east-west mean. In each case, T_{rot} was obtained from a Boltzmann analysis of CO line intensities (see text and Fig. 5), and uncertainties are based on 1 σ errors in the best fit slope. For each date, entries in bold refer to the ρ -range corresponding to the terminal portion of the Q-curve for CO. An increase of T_{rot} with ρ was seen on several dates, and this was particularly pronounced near perihelion (within R_h \sim 1.1 AU).

^d The larger uncertainties in T_{rot} on May 01 May result from traversal of a pocket of enhanced CO emission traversing the slit. Its rotation appears tied to that of the comet, and its study will be incorporated into a future publication.

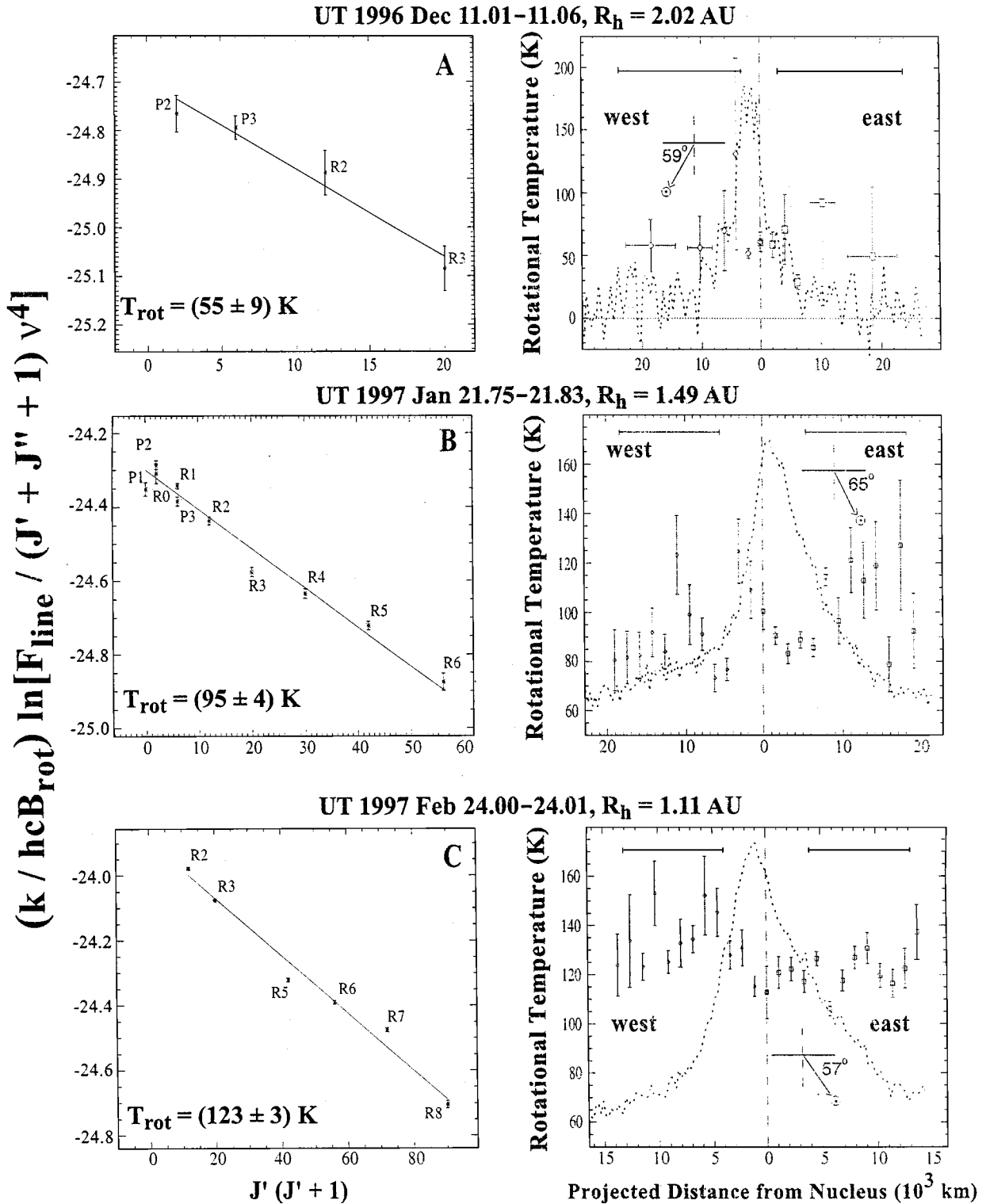


FIG. 5. CO excitation in the coma of Comet Hale-Bopp. *Left Panels:* Determination of rotational temperature (T_{rot}) based on the intensities of several CO lines (Eq. (1b)). For each date (plot), the east–west average of line fluxes collected over projected distances corresponding to the terminal region of the Q-curve for CO is used (see text, and Fig. 7). (This range in ρ is indicated by horizontal bars in each right-hand panel; cf Table II.) *Right Panels:* Rotational temperature (points, with 1σ error bars) as a function of projected distance from the nucleus. The general increase in T_{rot} with distance east and west of the nucleus is seen for CO on multiple dates, and appears most pronounced near perihelion. The dashed trace in each panel shows the overall spatial profile for CO, and $\rho = 0$ corresponds to the position of peak continuum emission (see Fig. 6). The zero intensity level for each CO profile is the bottom axis of the plot, with the exception of Dec. 11 and Aug. 08, for which it is given by the horizontal dotted line.

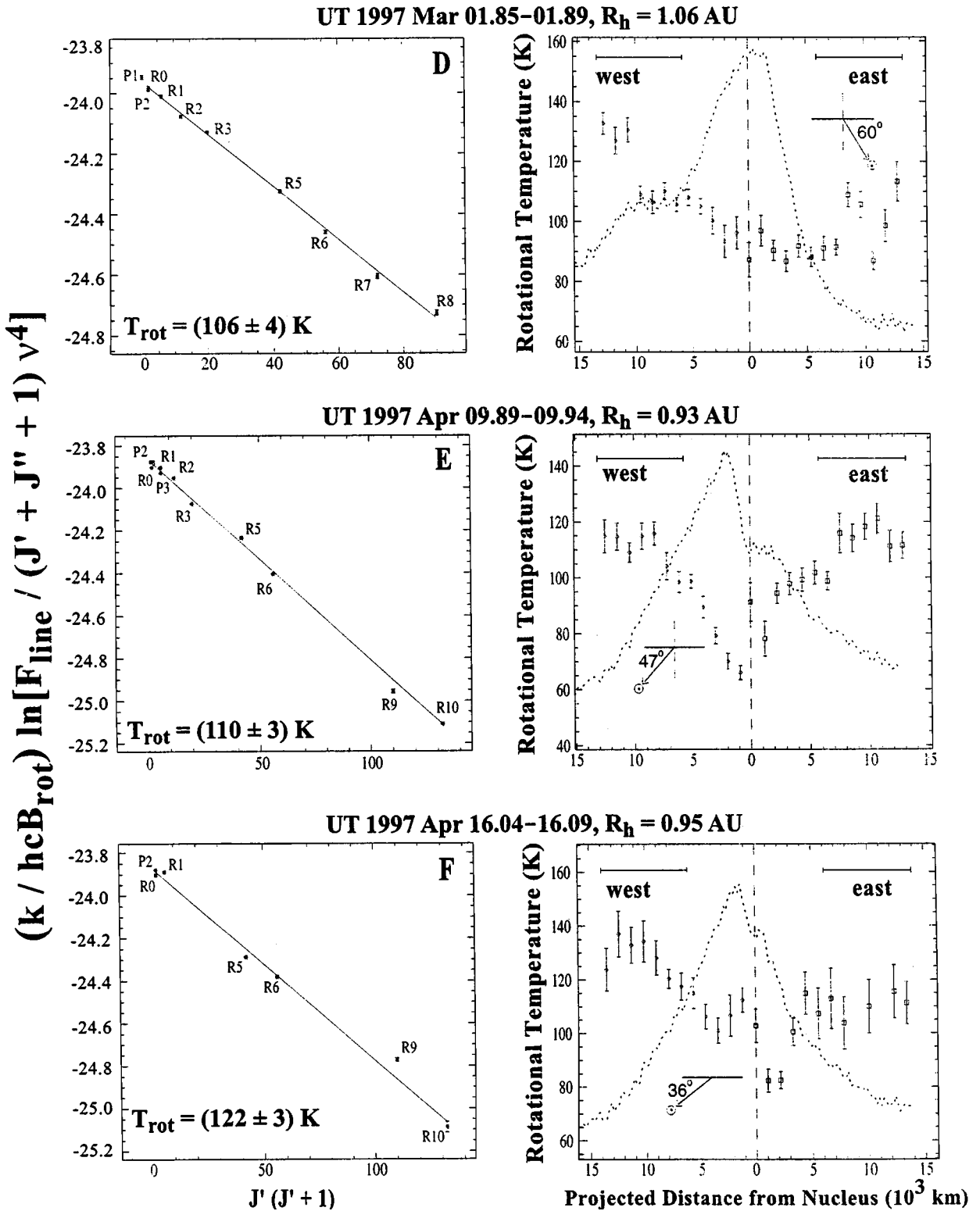


FIG. 5—Continued

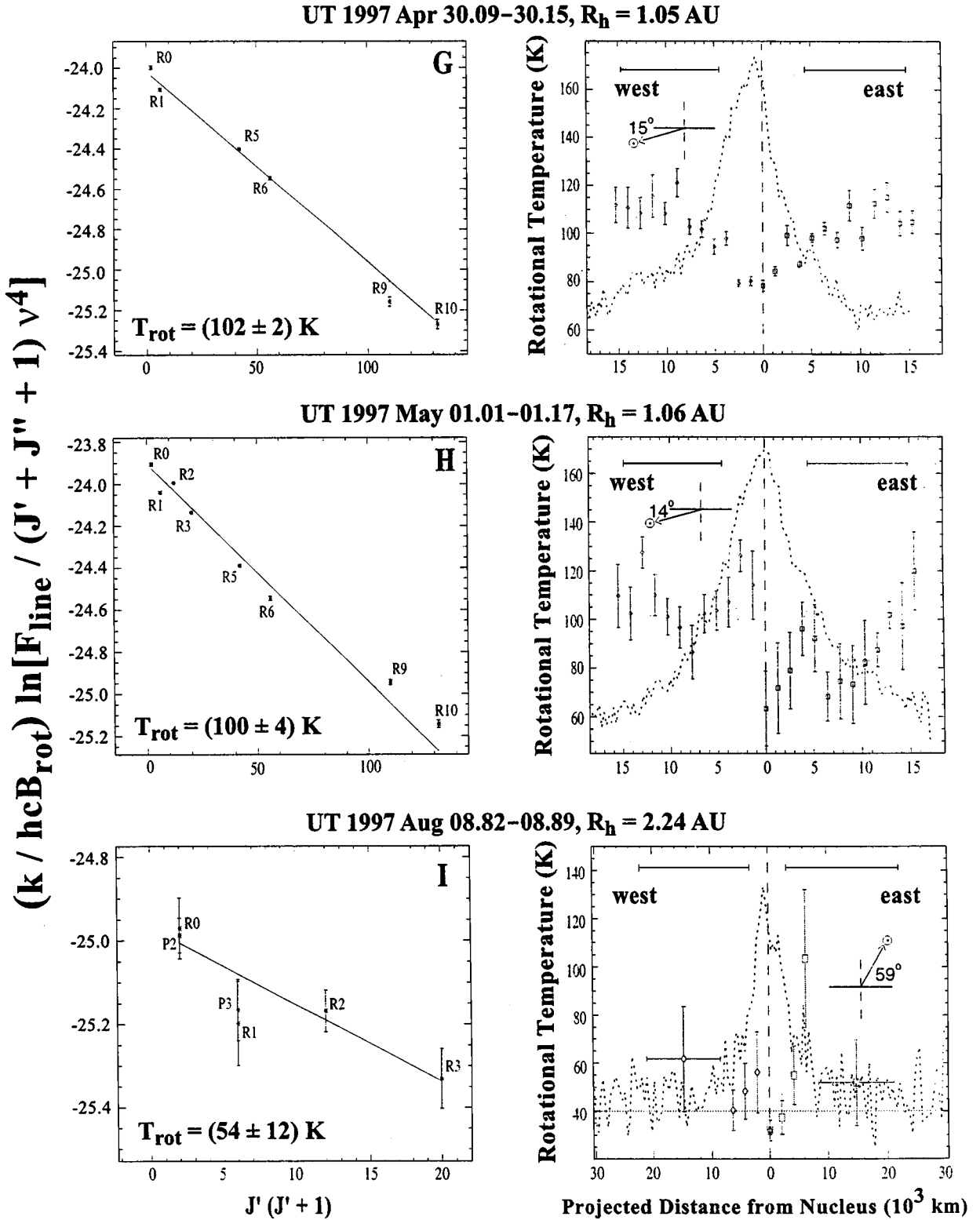


FIG. 5—Continued

between HCN and CO, this argues against control of rotational populations by radiative cooling, and could indicate control by collisions with electrons⁶ (Xie and Mumma 1992, Bockelée-Morvan *et al.* 1994, Biver *et al.* 1999a, Lovell *et al.* 2000). Recent observations of Comet 1999 H1 (Lee) also found the retrieved rotational temperatures for HCN and CO to be similar (~ 75 K; Mumma *et al.* 2001). The role of electrons should be relatively less important for CO owing to its small dipole moment. Biver *et al.* (1999a) successfully modeled line intensity maps of CO emission using neutral–neutral collisions alone, but electron collisions (and/or a significantly extended source) were required to reproduce line intensities in HCN, CS, and H₂CO.

If heating of the coma is controlled by photolytic and/or photoionization processes, then one might expect our measured rotational temperatures for CO to be correlated with both the production and distribution of water molecules in the coma.⁷ We note that our measured temperatures on UT 1997 February 24 were higher (~ 120 K) compared with those on most other dates (even for beams passing close to the nucleus), and that $Q_{\text{H}_2\text{O}}$ on this date was more than 2σ above the value predicted by its heliocentric power law fit (Dello Russo *et al.* 2000). Our future excitation studies will search for such correlations.

Our observed temperature profiles (T_{rot} versus ρ) can be compared with what might be expected from modeled profiles of gas temperature in the coma, when radiative cooling by water molecules is included in the calculations. A model developed by Bockelée-Morvan and Crovisier (1987) for comparison with observations of Comet Halley considered photolytic heating by fast H-atoms. Although they ignored heating from

⁶ Our derived rotational temperatures appear to be insensitive to the molecular dipole moment. For example, the dipole moment for CO ($\mu = 0.11$ Debye) is very small relative to that for HCN ($\mu = 3.0$ Debye; Lang 1980), yet we observe $T_{\text{rot}} \sim 100$ K (or somewhat higher) for each near $R_h = 1$ AU. This argues against control of rotational level populations by fluorescent pumping and radiative decay, at least in the region of the coma sampled by our observations. Instead, the dominant heating processes begin with destruction of water by solar ultraviolet and extreme ultraviolet photons. Photolysis (UV photons) produces fast H-atoms while photoionization (EUV photons) produces fast electrons. Both products cool mainly by collisions with neutral coma volatiles. Fast H-atoms lose their energy mainly by inelastic momentum transfer, heating the coma by thermalizing their excess kinetic energy. However, hot-electrons cool mainly by excitation of electronic, rotation–vibration, and pure-rotation transitions in ambient species. Ultimately, (radiative) rotational cooling of water thermostats the lowest energy electrons to a temperature similar to the rotational spacing in the ortho-ladder (~ 100 cm⁻¹, or ~ 70 K) (cf. Xie and Mumma 1992). Through collisions, these cool electrons control rotational excitation of other neutral species, such as CO and HCN. They eventually combine with ambient ions (mainly H₃O⁺) dissociatively, producing more fast H-atoms and still more heating.

⁷ Heating by electrons must occur through excitation of vibration and rotation (with subsequent V-T and R-T relaxation). Clearly, kinetic heating by electrons will mainly act through collisions with water owing to its dominant abundance and large dipole moment (and hence its large electron scattering cross section). Other species will play a lesser role. However, low-energy electrons will thermostat the water, and both will influence other species (through neutral–neutral or electron–neutral collisions).

dust (arguing it would have negligible effect for Halley; see also Bockelée-Morvan 1987) and electron heating, their predicted values for gas kinetic temperature (T_{gas}) and outflow speed were consistent with observations (Weaver *et al.* 1986, Mumma *et al.* 1986, Lämmerzahl *et al.* 1987). Bockelée-Morvan and Crovisier considered water production rates ranging from 10^{27} to 10^{30} molecules s⁻¹. For $Q_{\text{H}_2\text{O}}$ approaching 10^{29} s⁻¹ (and higher), their calculations predict an increase in T_{gas} from ~ 10 K near 100 km from the nucleus (well within our PSF) to typical values (several thousand km from the nucleus) which depend on $Q_{\text{H}_2\text{O}}$: i.e., $T_{\text{gas}} \sim 50$ K near 10^{29} s⁻¹, and $T_{\text{gas}} \sim 80$ K near 10^{30} s⁻¹. Extrapolating to water production rates $\sim 10^{31}$ s⁻¹ (as observed for Comet Hale-Bopp near $R_h = 1$ AU; Dello Russo *et al.* 2000), values of 100 K or higher (as seen in our profiles of rotational temperature for CO; Fig. 5) could be expected.

Further consideration of electron collisions is deferred to a future study, where we also will consider heating by dust. We will include analysis of step-map observations with the slit offset in the coma in directions perpendicular to its length (obtained on three dates) and parallel to its length (obtained on two dates). The perpendicular offset observations sample other parent molecules (e.g., H₂O and C₂H₆) in addition to CO, and provide a two-dimensional picture of coma gas and (μm -sized) dust morphology. The parallel offset (or “extended slit”) observations extend our spatial coverage of CO emission to $\sim 4\text{--}5 \times 10^4$ km from the nucleus.

Our mapping observations provide a measure of CO rotational temperature along the slit at each position. These data will establish whether a correlation exists between regions of enhanced CO emission in the coma (e.g., arising from jets; see below) and higher values of T_{rot} . Our analysis to date suggests that such a correlation is possible (e.g., Figs. 5D and 5E, right-hand panels). If verified, this could indicate that CO produced in the coma plays a role in heating the coma, for example through increased collisions with electrons. However, this is expected to be less efficient than collisions of electrons with water, because of the small dipole moment of CO. Our step-mapping observations may also help to explain differences seen in our temperature profiles on different dates, i.e., why we see a strong degree in heating on some dates, while it appears weak or essentially absent on others. We do not yet understand the cause of these differences.

DISTRIBUTION AND RELEASE OF CO

The overall spatial distribution of CO molecules in the coma is revealed by combining spatial profiles for lines that sample a range of rotational states. Representative spatial profiles are shown for various heliocentric distances in Fig. 6. Each panel compares the distribution of CO emission with that from volatiles released solely from the nucleus (H₂O or C₂H₆). Figure 6A shows that the profiles for CO and C₂H₆ were of similar extent near 2 AU perihelion, while the dust displayed

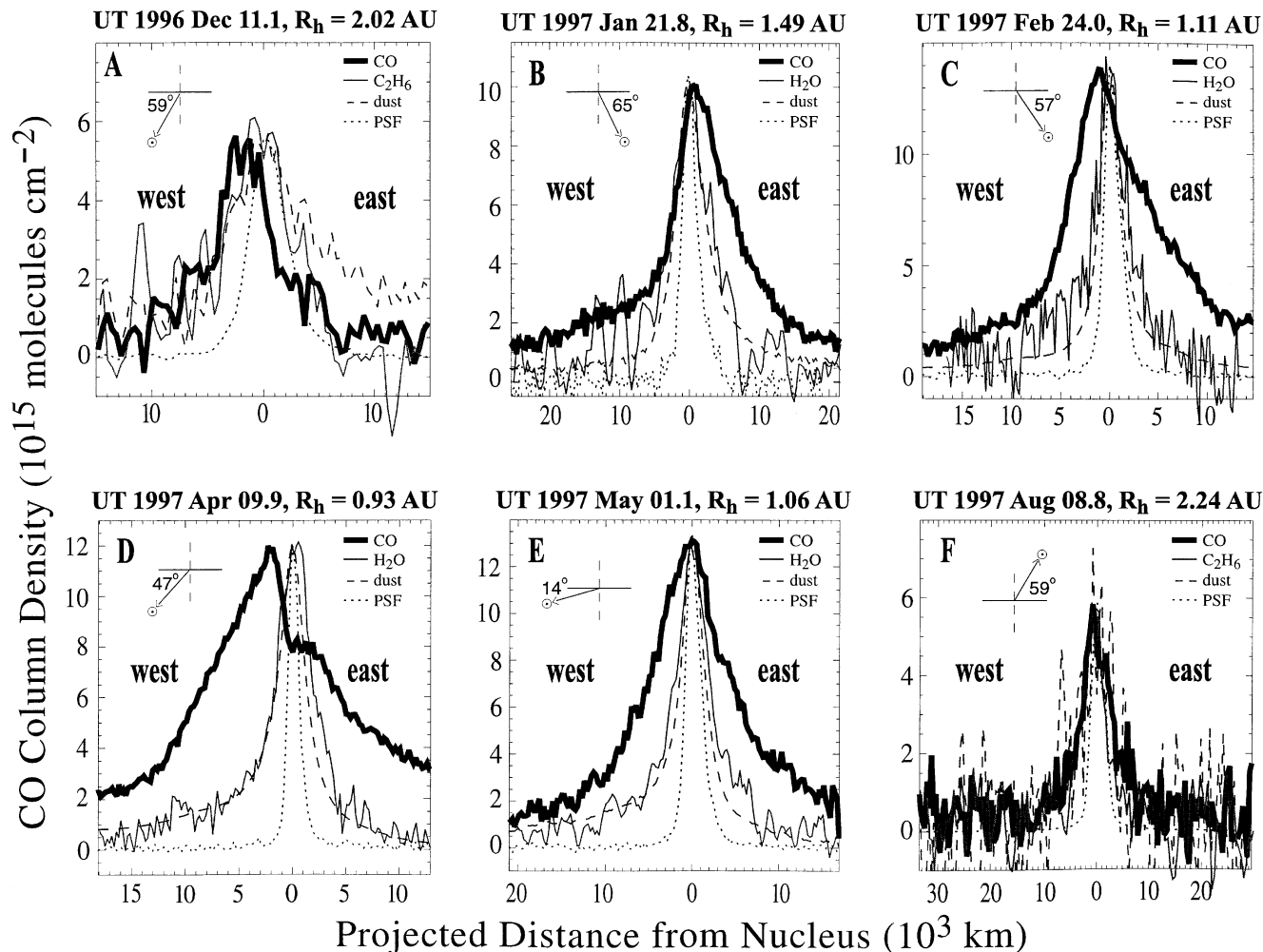


FIG. 6. Spatial profiles of CO emission in comet Hale-Bopp on three preperihelion (panels A–C) and three postperihelion (panels D–F) dates. Shown in each panel is the sum of line profiles sampling a range in rotational levels, thereby providing a measure of the overall CO distribution in the coma. Also shown are scaled parent volatile (C_2H_6 or H_2O , light trace), continuum (dashed trace) and stellar (“point spread function,” dotted trace) profiles. Note the change in appearance between December and January CO profiles, which we take to signal the onset of the distributed source (see text for detailed discussion). This shows the power of combining high-spatial and high-spectral resolution, as afforded by CSHELL.

pronounced asymmetry toward the anti-sunward hemisphere (perhaps because of solar radiation pressure). However, within 1.5 AU, the CO profile consistently exhibited a markedly more extended distribution than either water or dust in both east and west directions (Figs. 6B–6E). (An extended CO distribution was also reported from independent CSHELL observations of Comet Hale-Bopp obtained on UT 1997 March 05 ($R_h = 1.03$ AU preperihelion); Weaver *et al.* 1999.) At 2.24 AU postperihelion, CO, C_2H_6 , and dust were east–west symmetric and their profiles had the same extent and shape (Fig. 6F). If CO were released only from the nucleus, its profile should mimic those for native species such as H_2O and C_2H_6 . The much broader extent for CO that appeared near (and persisted within) 1.5 AU of the Sun is suggestive of the presence of a second (distributed) source.

Evidence of both native and distributed CO contributions can be seen by examining the apparent “spherical” production rate (Q , molecules s^{-1}) as a function of line-of-sight distance from the nucleus (Magee-Sauer *et al.* 1999; Dello Russo *et al.* 1998, 2000). This may be derived from the intensity measured at a specific location, using the (idealized, but useful) assumption of uniform spherical outflow from the nucleus,

$$Q = \frac{4\pi \Delta^2 \Sigma F_{line}}{h\nu (\tau \Sigma g_{line})_{1AU} f(x)}, \quad (2)$$

where Δ (m) is the geocentric distance, $h\nu$ is the energy per photon (J), and τ and g_{line} are the CO photo-dissociation lifetime (s) and line fluorescence g -factor (photon s^{-1} molecule $^{-1}$),

respectively.⁸ The quantity $f(x)$ represents the fraction of the total number of CO molecules contained within the sampled region (initially developed by Yamamoto (1982) for a circular nucleus-centered aperture; see Appendix of Hoban *et al.* 1991 regarding calculation of $f(x)$ for square pixels lying along a slit). For offsets significantly smaller than one scale-length ($v\tau$), the function $f(x)$ ($\ll 1$) varies approximately as τ^{-1} , hence our derived values of Q are nearly independent of the assumed destruction lifetime for the observed species. The summations for F_{line} and g_{line} extend over the measured CO lines.

Spherical production rate curves (Q-curves) are generated by stepping a 1×1 arcsecond aperture along the emission profile (along the slit) and extracting Q at one arcsecond intervals. A “symmetrized” production rate is obtained by averaging Q east and west of the nucleus (Fig. 7). Analogous Q-curves are generated for dust by stepping along the corresponding continuum profile, assuming the scale length for dust to be long compared with the projected length of the slit at the comet. Production rates derived in this manner invariably increase from a minimum at the nucleus to a steady-state (or terminal) value at some distance from the nucleus. We take the terminal value to represent the total production rate (Table III). Through comparison with Q-curves generated from a representative stellar profile convolved with a ρ^{-1} function (i.e., the convolved point spread function), we have demonstrated that Q-curves for species having a purely native source show an increase primarily because of seeing (e.g., water (Dello Russo *et al.* 2001), hydrogen cyanide (HCN; Magee-

⁸ We use $\tau(\text{CO}) = 1.335 \times 10^6 R_{\text{h}}^2$ s (for quiet Sun conditions; Huebner *et al.* 1992), where R_{h} is in AU. The fluorescence efficiency $g_{\text{line}} = n_{1,J'} A_{J',J''}$, where $n_{1,J'}$ is the fractional population of CO molecules in the upper state ($v' = 1, J'$). Since $n_{1,J'}$ is a function of rotational temperature (see footnote 5, and also Crovisier 1987, Chin and Weaver 1984, Weaver and Mumma 1984), Q is also dependent on T_{rot} , although not strongly so provided the distribution of CO rotational levels is adequately sampled, as was the case for our Hale-Bopp observations (cf Tables I and III). The band g-factor represents the sum over all g_{line} in both P- and R-branches,

$$g_{\text{band}} = n_{1,0} A_{0,1} + \sum_{J' > 0} n_{1,J'} (A_{J',J'+1} + A_{J',J'-1}),$$

where $A_{0,1}$ is the transition probability for emission in the P1 line (P1 provides the only means of testing the population in $J' = 0$). $A_{J',J'+1}$ and $A_{J',J'-1}$ are transition probabilities for emission in P- and R-branch lines, respectively, having a common upper state. The value of g_{band} for CO ($\sim 2.6 \times 10^{-4}$ photon s^{-1} molecule $^{-1}$ at $R_{\text{h}} = 1$ AU, Chin and Weaver 1984) is independent of rotational temperature, except when the population is relaxed to $J'' = 0$ and 1, such as at very low rotational temperature (in which case detailed balancing must be applied; see Chin and Weaver 1984 for details). The relation governing the total column density in $v' = 1$ is approximated as

$$N_1 \cong N_0 g_{\text{band}} (A_J)^{-1} = N_0 g_{1,\text{band}} R_{\text{h}}^{-2} (A_J)^{-1},$$

where N_0 is the column density in $v = 0$, $g_{1,\text{band}}$ is the $1 - 0$ band fluorescence efficiency at 1 AU heliocentric distance, and A_J is the total transition probability for ro-vibrational emission from a given upper state. A_J ($\approx 33 \text{ s}^{-1}$) is nearly independent of J' , since S_J is independent of J' when contributions from P- and R-branch lines are summed. This value also holds for A_0 , even though relaxation of this level can proceed only through P1 (i.e., $A_0 \equiv A_{\text{P1}}$).

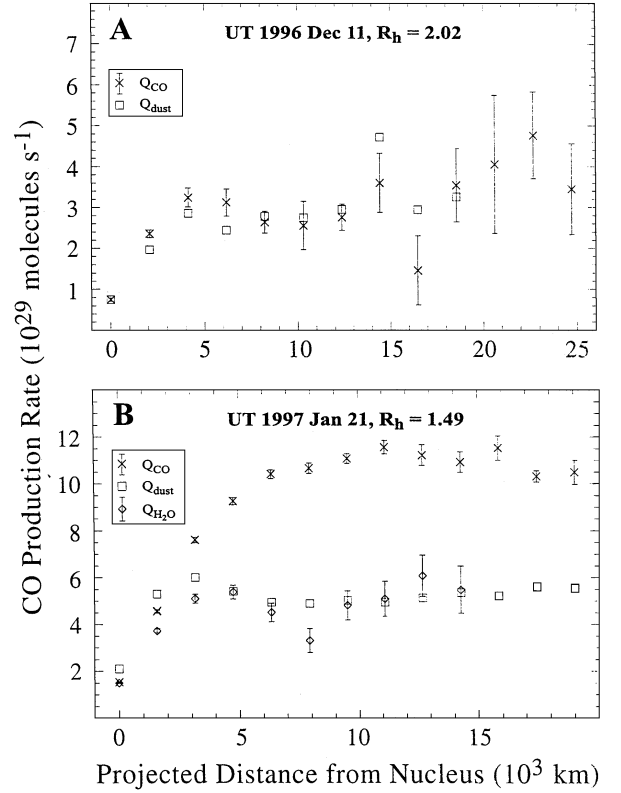


FIG. 7. Production rate curves (Q-curves) for Comet Hale-Bopp, showing the measured Q as a function of line-of-sight (i.e., projected) distance from the nucleus. An aperture (1×1 arcsecond) is stepped along the spatial profile of CO and the flux is measured at each position. Production rates are calculated from the (symmetrized) line flux (F), and from the fraction of the total CO in the coma expected to be contained in the beam assuming production at the nucleus and uniform outflow in the coma [$f(x)$ in Eq. (2)]. At each position (step), the average of Q east and west of the nucleus is plotted. Q_{CO} values are denoted by the symbol “x,” with 1σ error bars shown. For comparison, the corresponding continuum Q-curve (open squares) is also shown, generated by assuming a scale length for the dust which is large compared with the projected length of the slit at the comet. Each continuum Q-curve has been scaled to the level of the CO Q-curve at the approximate distance from the nucleus where the CO emission becomes optically thin. In December 1996 (panel A, $R_{\text{h}} = 2.02$ AU), this distance falls within the central pixel. In January 1997 (panel B, $R_{\text{h}} = 1.49$ AU), we estimate this distance to occur $\sim 1,800$ km from the nucleus (see Appendix), and terminal values of Q-curves for scaled continuum (or H_2O , open diamonds) and CO are in the ratio 0.49 (consistent with the ratio of native to total CO our analysis predicts for this R_{h} ; Table III). This figure suggests a strong contribution from the distributed CO component in January (excess of total CO over scaled continuum or water Q-curve) which was not present in the December data.

Sauer *et al.* 1999), or ethane (C_2H_6 ; Dello Russo *et al.* 2001)). Our Q-curves for CO outside $R_{\text{h}} \sim 2$ AU are consistent with a purely native source.

The evolution from a purely native source for CO to a combination of native and distributed components occurred between 1996 December 11 (2.02 AU preperihelion) and 1997 January 21 (1.49 AU preperihelion) and is clearly seen by comparing Q-curves for these dates (Fig. 7). When release is solely from the nucleus, the Q-curve reaches its terminal value quickly; in

TABLE III
CO Production Rates in C/1995 O1 Hale-Bopp

UT Date ^a	R _h	ρ -range ^b	T _{rot} (K) ^c	%v' = 1 ^d	%Band ^d	Q _{CO} ^e	Q _{Nat} ^f	Q _{CO} /Q _{H₂O} ^g	Q _{Nat} /Q _{H₂O} ^h	Q _{Dist} ⁱ
1996										
Jun 13.54–13.59	4.10		20	35.3	26.9	0.96 ± 0.15	0.96 ± 0.15			—
Sep 19.22–19.23	3.03		30	43.6	27.4	1.28 ± 0.26	1.28 ± 0.26			—
Dec 11.01–11.06	2.02	1.5–11.5 (3.09–23.69)	55 ± 9	64.6	33.9	2.98 ± 0.32	2.98 ± 0.32			—
1997										
Jan 21.74–21.83	1.49	3.5–11.5 (5.55–18.25)	95 ± 4	83.7	50.0	10.78 ± 0.30	5.32	0.267 ± 0.029	0.131 ± 0.014	5.46 ± 0.40
Feb 23.99–24.01	1.11	3.5–11.5 (4.00–13.14)	122 ± 3	58.6	26.6	18.16 ± 0.75	8.83	0.241 ± 0.016	0.117 ± 0.008	9.33 ± 0.80
Mar 01.85–01.89	1.06	5.5–12.5 (5.89–13.38)	106 ± 4	79.3	40.7	19.80 ± 0.57	9.58	0.271 ± 0.011	0.131 ± 0.005	10.22 ± 0.63
Apr 09.88–09.93	0.93	5.5–12.5 (5.77–13.10)	110 ± 3	69.7	41.1	22.31 ± 1.35	12.06	0.276 ± 0.022	0.148 ± 0.012	10.25 ± 1.38
Apr 16.04–16.09	0.95	5.5–12.5 (6.13–13.92)	122 ± 3	43.5	23.1	24.69 ± 2.04	11.61	0.297 ± 0.028	0.139 ± 0.013	13.08 ± 2.06
Apr 30.09–30.15	1.05	3.5–11.5 (4.46–14.65)	102 ± 3	50.6	18.6	14.27 ± 1.00	9.74	0.222 ± 0.023	0.150 ± 0.015	4.53 ± 1.04
May 01.01–01.17	1.06	3.5–11.5 (4.51–14.82)	100 ± 4	70.8	30.5	17.93 ± 0.87	9.57	0.280 ± 0.024	0.149 ± 0.013	8.36 ± 0.91
Aug 08.80–08.91	2.24	1.5–10.5 (3.17–22.17)	54 ± 12	65.1	45.5	2.95 ± 0.37	2.95 ± 0.37			—
Sep 25.65–25.74	2.83		30	45.6	18.7	1.45 ± 0.33	1.45 ± 0.33			—

^a Time interval over which CO observations included in the present analysis were obtained, in decimal UT date.

^b Range of projected distances ρ over which the CO production rate was determined (i.e., the terminal portion of the Q-curve), in arcseconds, and in thousands of km (in parentheses).

^c CO rotational temperature, measured over the terminal portion of the Q-curve, and averaged east and west of the nucleus. For the three dates (all with R_h > 2.8 AU) not having ρ -values, the rotational distribution was not adequately sampled, hence T_{rot} was adopted from Fig. 1 of Biver *et al.* 1997, and an uncertainty in rotational temperature (± 5 K, 1σ) has been included in calculating Q_{CO} for these dates.

^d “%v' = 1” is the percentage of the upper vibrational state population sampled by the measured CO lines at rotational temperature T_{rot}. “%Band” is the percentage of the total COv = 1 – 0 band g-factor ($\sim 2.6 \times 10^{-4}$ photon s⁻¹ molecule⁻¹) represented by the lines measured, also at T_{rot}. Thus, for example at T_{rot} = 20 K, our 1996 June 13 observations of the P1 and P2 lines sampled 35 percent of the population in v' = 1, and their combined g-factor was (0.269)(2.6 × 10⁻⁴)(4.1)⁻² $\sim 4.2 \times 10^{-6}$ photon s⁻¹ molecule⁻¹.

^e Total observed CO production rate (10²⁹ molecules s⁻¹). For each date, Q was calculated line-by-line using g-factors appropriate to the derived rotational temperature. Q_{CO} represents the average for all lines observed, and listed uncertainties represent 1 σ errors. For R_h > 2 AU, where only native CO was seen, this is dominated by the stochastic error. For R_h < 1.5 AU, line-to-line variations in derived Q generally dominate the stochastic error, and hence σ . In all cases Q incorporates 14–20 points per line, and multiple lines per date (cf. Fig. 7). Since we rely on terminal Q-curve values, this method is independent of possible effects in the inner coma (e.g., CO optical depth; see Appendix).

^f Production rate for that fraction of the total CO stored as ice in the nucleus (10²⁹ molecules s⁻¹). On the dates for which (1 σ) uncertainties are listed, the spatial profile of CO emission was consistent with a ρ^{-1} distribution convolved with the instrumental point spread function, suggesting that only the native CO source was active at heliocentric distances R_h > 2AU. For R_h < 1.5 AU (Jan 21–May 01), we list values extrapolated from the “native” fit (see Fig. 8), and assume a 1 σ uncertainty of $\pm 0.030 \times 10^{29}$ for each point, corresponding to the approximate RMS scatter about the fit.

^g Total Q_{CO} relative to H₂O (water production rates after Dello Russo *et al.* 2000). The mean total CO mixing ratio for these dates was 0.241 ± 0.009.

^h Inferred production of native CO relative to H₂O, based on the (extrapolated) native CO heliocentric fit (Fig. 8). The mean value for these dates was 0.124 ± 0.004. Thus, the mean fractional abundance of native CO to total CO was 51 ± 3%.

ⁱ Production rate for that fraction of the total CO produced in the coma, 10²⁹ molecules s⁻¹. Q_{Dist} is represented by the difference between total and extrapolated native CO contributions (columns g and h, respectively), and obeys a heliocentric power law Q_{Dist} = (1.02 × 10³⁰) R_h^{-1.57±0.41} with 1 σ RMS scatter of $\pm 1.44 \times 10^{29}$ molecules s⁻¹ about the fit. While active, the mean derived production rate relative to H₂O for distributed CO was Q_{Dist}/Q_{H₂O} = 0.117 ± 0.022.

this case the Q-curves for CO and dust have similar shapes (Fig. 7A). However, when both native and distributed sources are present (as is the case for CO, Fig. 7B), the Q-curve reaches its terminal value farther from the nucleus. The ratio of contributions from native and distributed sources may be estimated by comparing the Q-curve for CO with those generated from profiles of purely native species (Fig. 7B). The Q-curves shown for water and dust represent proxies for the native CO source alone,

and they provide additional support for the existence of both distributed and native sources of CO in Comet Hale-Bopp for R_h < 1.5 AU.

Since our model assumes constant outflow velocity, acceleration in the intermediate coma could influence the shapes of our Q-curves. Can this account for the observed behavior of the Q-curves for CO within ~ 1.5 AU of the Sun? The gas outflow velocity (v_{gas}) in Comet Halley (at R_h ~ 0.90 AU

postperihelion) was nearly constant ($0.80 \pm 0.05 \text{ km s}^{-1}$) between distances of approximately 1,000 km and 4,000 km from the nucleus, but v_{gas} increased by ~ 25 percent between 4,000 km and 20,000 km (Lämmerzahl *et al.* 1987). We tested the sensitivity of our retrievals to such acceleration by assuming a similar velocity increase for Hale-Bopp; only modest enhancements in Q_{CO} (~ 3 –4% at 1.49 AU, and ~ 6 –8% near perihelion) were obtained.

Based on the neutral gas acceleration predicted by a dusty gas hydrodynamic model run for our observations at $R_h = 1.49 \text{ AU}$ (D. Boice, personal communication; see also Boice *et al.* 1998, Boice and Watanabe 1999), we expect inclusion of a non-uniform gas velocity profile to have little effect on our retrieved production rates. This is because the initial steep increase in v_{gas} occurs within about 100 km of the nucleus, and this is well within our PSF. Our determination of Q_{CO} is most sensitive to the region 5 – $20 \times 10^4 \text{ km}$ from the nucleus, yet this model predicts (as do other coma models; see also Bockelée-Morvan and Crovisier 1987, Combi *et al.* 1999) a more gradual acceleration between about 100 km and 2 – $3 \times 10^4 \text{ km}$ from the nucleus, beyond which the acceleration increases more steeply. We therefore expect nonuniform outflow velocities to introduce only small corrections to our retrieved production rates. Gas acceleration will be incorporated into our future work, for not only refining production rates, but also for further assessment of optical depth effects (see Appendix), and for studies of observed asymmetry in the outflow.

Regardless of the magnitude of these refinements, Q -curves for species released at the nucleus (e.g., H_2O and native CO) should be affected similarly by acceleration. The Q -curves for water and dust are nearly identical in shape, but they differ greatly from those of CO inside 1.5 AU heliocentric distance (Fig. 7B). While acceleration could introduce small increases to our retrieved gas production rates, another cause must be sought for the strong difference between Q -curves for water and CO. Again, this suggests the presence of a distributed source for CO, similar to that found for 1P/Halley (Eberhardt *et al.* 1987, Eberhardt 1999).

HELIOCENTRIC DEPENDENCE

The dependence of total CO production rate on heliocentric distance can also be used to discriminate native and distributed sources of CO in Comet Hale-Bopp, and to estimate the contributions from each (Fig. 8). Our production rates for $R_h > 2 \text{ AU}$ are consistent with $Q_{\text{Nat}} = 1.06 \times 10^{30} R_h^{-1.76 \pm 0.26} \text{ molecules s}^{-1}$. We take this to represent the (purely) native contribution to total CO, based on the similar spatial shapes for CO and parent volatiles (e.g., C_2H_6 or H_2O ; cf Fig. 6). This heliocentric dependence is consistent with that derived for H_2O using the same instrument and approach, and analysis of our water profiles supports its release primarily as a parent volatile from the nucleus (Dello Russo *et al.* 2000). A similar heliocentric dependence was found for large (mm-sized) dust over the range

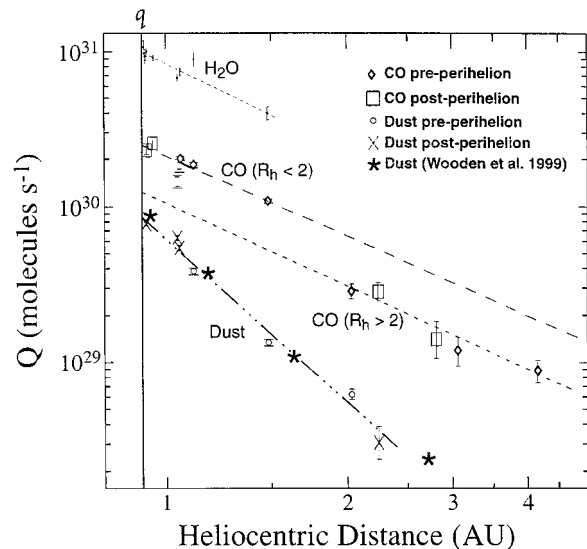


FIG. 8. Heliocentric dependence of CO production rates in comet Hale-Bopp, with error bars indicating 1σ uncertainties. The preperihelion discontinuous increase in Q_{CO} between 2.0 and 1.5 AU is evident. A least squares linear fit to dates with $R_h > 2 \text{ AU}$ is used to approximate the contribution from native CO (short-dashes); this has a power law slope of -1.76 ± 0.26 . A fit to dates with $R_h < 2 \text{ AU}$ (long-dashes) reveals a similar slope (-1.66 ± 0.22). These fits imply values at $R_h = 1 \text{ AU}$ of $(1.06 \pm 0.44) \times 10^{30}$ and $(2.07 \pm 0.20) \times 10^{30} \text{ molecules s}^{-1}$, respectively. Values of $Q_{\text{H}_2\text{O}}$ obey a power law fit with slope $= -1.88 \pm 0.18$ (Dello Russo *et al.* 2000). We take this similarity in heliocentric dependence to indicate that the overall (long-term) release of native CO, of the distributed CO “parent” species, and of water are all controlled by sublimation of the same nuclear ice (see text). Extrapolating the $R_h > 2 \text{ AU}$ fit to smaller heliocentric distances permits an estimate of contributions from the two CO sources (Table III). The relative dust production obeys a much steeper power law (-3.62 ± 0.13), and exhibits no discontinuity between 2.0 and 1.5 AU comparable to that seen for CO. This indicates that the onset of distributed CO cannot be explained in terms of increased dust production alone, rather a thermal threshold for release of the distributed parent seems likely. The vertical solid line (indicated by q) marks the perihelion distance for Hale-Bopp (0.914 AU).

$0.9 \text{ AU} < R_h < 2.5 \text{ AU}$ (Jewitt and Matthews 1999), and these larger particles represent the bulk of the total dust mass lost by Hale-Bopp (this differs from the heliocentric dependence for production of μm -sized dust; see below).

A separate fit for $R_h < 2 \text{ AU}$ [$Q_{\text{CO}} = 2.07 \times 10^{30} R_h^{-1.66 \pm 0.22}$] shows the same heliocentric dependence, and is displaced above the “native” fit by a factor of ~ 2 . Thus, our data suggest native and distributed sources contribute about equally to the total CO production in Comet Hale-Bopp within 1.5 AU of the Sun (Table III). We note that our estimated native Q_{CO} values for $R_h < 1.5 \text{ AU}$ (based on extrapolation of the native fit to smaller R_h) are consistent with those inferred from our scaled (continuum or water) Q -curves. For example, in Fig. 7B the two innermost points for CO lie somewhat below the corresponding continuum points. This is consistent with some degree of optical trapping in the CO lines along lines-of-sight near the nucleus; however, this has only a minor influence on our measured production rates for CO since these are based on signal taken much

farther from the nucleus, where opacity effects are minimal (e.g., over the range $\rho \sim 5,500 - 18,000$ km on UT 1997 January 21; see Appendix).

We also examined our data for evidence of a sudden change in (μm -sized) dust production within 2 AU of the Sun, similar to that seen for CO. Had a second nuclear vent become activated between 1.5 and 2 AU, a step-like increase in dust production might be expected. The relative production of μm -sized dust (Q_{dust}) was determined from our measured continuum flux density F_{ν} (watts $\text{m}^{-2}/\text{cm}^{-1}$) after distinguishing contributions from grain thermal emission [$F_{\nu}(\text{th})$] and scattered sunlight (see Table III of DiSanti *et al.* 1995 for formalism). We used our spectroscopic observations near 2.0, 3.35, and 4.7 μm , for this analysis. Q_{dust} is dependent upon the surface area of μm -sized grains, which represent a very small fraction of the total dust mass. Values for Q_{dust} are given by $F_{\nu}(\text{th})/B_{\nu}(T_{\text{dust}})$, averaged over CO settings. The Planck function $B_{\nu}(T)$ varies as $\nu^3/[\exp(hc\nu/kT) - 1]$, and we take $T(\text{K}) \equiv T_{\text{dust}} = 400R_{\text{h}}^{-0.5}$ based on thermal infrared ($\lambda \sim 10 \mu\text{m}$) observations of Comet Hale-Bopp by Wooden *et al.* (1999).

Our observed Q_{dust} obeys a considerably steeper power law ($R_{\text{h}}^{-3.62 \pm 0.13}$; see Fig. 8) than does the release of CO, H_2O , or mm-sized dust, but it is close to the power law we estimate for the 10- μm dust ($\sim R_{\text{h}}^{-3.35}$, based on thermal continuum intensities reported by Wooden *et al.* 1999). (Our derived heliocentric dependence for Q_{dust} is steeper than that reported in DiSanti *et al.* 1999 ($R_{\text{h}}^{-2.73 \pm 0.12}$), since there we assumed $T_{\text{dust}} = 329R_{\text{h}}^{-0.53}$ based on infrared measurements of Comet Halley (Green *et al.* 1986).) We see no discontinuous increase in the production of micron-sized dust between $R_{\text{h}} = 2.0$ and 1.5 AU that might correlate with the jump seen for CO (Fig. 8), nor do we see a discontinuity in ethane production, which we measured over the range $0.92 \leq R_{\text{h}} \leq 2.83$ AU (Dello Russo *et al.* 2001). Although several lines of evidence support this interpretation, some caution in interpreting heliocentric dependences should be exercised as a result of significant gaps in our heliocentric coverage of Comet Hale-Bopp.

The amount of CO produced in the coma (Q_{Distr}) is represented by the difference between Q_{CO} measured for each date (for $R_{\text{h}} < 2$ AU) and the value taken from the extrapolated power law fit to the native source (Q_{CO} for $R_{\text{h}} > 2$ AU) (see Table III). This difference ($Q_{\text{Distr}} = 1.02 \times 10^{30} R_{\text{h}}^{-1.57 \pm 0.41}$) obeys a power law consistent with that found for water (Dello Russo *et al.* 2000), native CO, and mm-sized dust particles (Jewitt and Matthews 1999).

RELATIVE CO ABUNDANCE

The heliocentric dependences derived for native CO and distributed CO agree with that found for water. Hence, we infer a nearly constant mixing ratio (relative to H_2O) for CO contained as ice in the nucleus, and also for the progenitor(s) of distributed CO in Comet Hale-Bopp. In Table III, we list the production rates of total CO (Q_{CO}), of Q_{Nat} , and of Q_{Distr} . When averaged

over the range $R_{\text{h}} = 1.49$ AU preperihelion through 1.06 AU postperihelion, the mixing ratios for Q_{CO} and Q_{Nat} are 24.1 ± 0.9 percent and 12.4 ± 0.4 percent, respectively (Table III). This indicates that approximately one-half (51 ± 3 percent) of the total carbon monoxide is present as CO ice in the nucleus. The derived mixing ratio for the distributed component alone is 11.7 ± 2.2 percent.

Nature of the Distributed CO

The difference between Q-curves for CO and μm -sized dust or H_2O (cf Figs. 7B and A4) approximates the Q-curve for the distributed component alone. The production of distributed CO reaches its terminal value at a projected distance $\rho \sim 6-7 \times 10^3$ km from the nucleus when $R_{\text{h}} = 1.49$ AU (see also Fig. A4), and at $\rho \sim 5 \times 10^3$ km when $R_{\text{h}} = 1.06$ AU. These projected distances approximate the scale for release of distributed CO; however, they should be considered lower limits for the scale length of its progenitor species. Determination of the progenitor scale length requires modeling the coma outflow (including asymmetries), and consideration of observing geometry. This should include a rigorous treatment of the volume emission rate at each point along the beam and a three-dimensional outflow model. This is deferred to a future paper, which will incorporate our coma step-mapping observations (see above). We expect such modeling to have relatively little effect on our retrieved production rate for native CO, yet it may provide significant improvements to our understanding of the distributed source.

Our derived production rates for CO and water exhibit scatter about their respective heliocentric power law fits (Fig. 8), and that scatter contains information about short-term variations in cometary activity. We first remove longer term changes (i.e., with heliocentric distance) by expressing the *relative* production rates ($Q_{\text{rel}} = Q/Q_{\text{fit}}$), where Q_{fit} is taken from the appropriate power law fit. The scatter in Q_{rel} then is a meaningful measure of (proportional) short-term variability (Fig. 9). Two parameters are of interest—the stochastic measurement error (σ_s) and the variance about the fit (σ_v) (Table IV). The scatter associated with the individual stochastic measurement errors ($\sigma_s \equiv (\sum \sigma_i^2)^{1/2}$) approximates the stochastic error associated with each distribution. The scatter derived from the weighted variance of each point from the fit ($\sigma_v \equiv (N/(N-1))^{1/2} (\sum (Q_{\text{rel},i} - Q_{\text{rel,mean}})^2 / \sigma_i^2)^{1/2} / (\sum 1/\sigma_i^2)^{1/2}$) expresses the degree to which the measurements deviate from the power law fit. Their ratio (σ_v/σ_s) is a measure of the degree to which stochastic errors alone contribute to the variance. The σ_i (error bars in Fig. 9) approximate the (1σ) stochastic error associated with point ‘i’, N is the total number of points (i.e., dates on which Q was measured), $Q_{\text{rel,mean}}$ is the weighted mean value of Q_{rel} ($Q_{\text{rel,mean}} \sim 1.0$), and the summations run from $i = 1$ to N . Thus, σ_v/σ_s provides a measure of the actual scatter of each distribution relative to its stochastic error.

Results are given in Table IV. For the five dates with $R_{\text{h}} > 2$ AU (when only the native CO component was present), and for the ten dates on which we measured H_2O (all within $R_{\text{h}} = 1.5$ AU; Dello Russo *et al.* 2000), $\sigma_v/\sigma_s < 1$; i.e., we see no

evidence for short term variability in either water within 2 AU or native CO beyond 2 AU. However, $\sigma_v/\sigma_s > 1$ for CO within 1.5 AU, both for total CO (the sum of native and distributed sources; Fig. 9A) and for the distributed component alone (Q_{Distr}; Fig. 9B). Taken together with the variable and frequently complex structure exhibited by our spatial profiles for CO (see, e.g., Fig. 6D), this apparent increased variability could result from nonuniformities in the source function for the distributed component (see below).

DISCUSSION

Because of its high volatility, CO is a sensitive indicator of the degree of heating experienced in the nebula and proto-solar environment. A comparison of our derived mixing ratio for CO

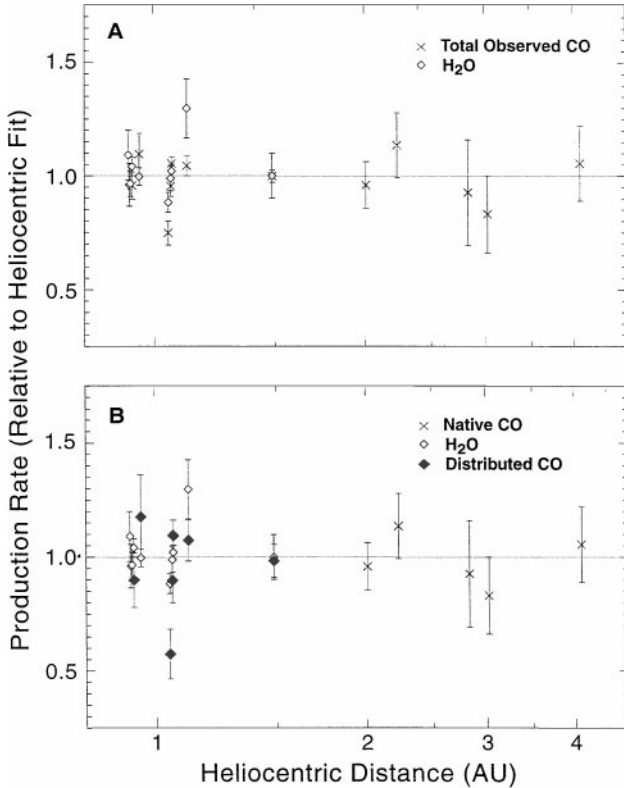


FIG. 9. Derived production rates of total CO (x’s), water (open diamonds), and distributed CO (filled diamonds), divided by their respective heliocentric power law fits from Fig. 8. Panel A: x’s refer to purely native CO outside $R_h = 2$ AU, and to combined native plus distributed CO within 1.5 AU. Panel B: x’s are identical to those in panel A outside 2 AU. Filled diamonds represent Q_{Distr} divided by $1.02 \times 10^{30} R_h^{-1.57}$ (see text). Open diamonds in both panels correspond to our measured $Q_{\text{H}_2\text{O}}$ divided by $8.35 \times 10^{30} R_h^{-1.88}$ (Dello Russo *et al.* 2000). Error bars indicate 1σ uncertainties, and include stochastic noise plus line-to-line variations in derived Q . For CO outside 2 AU, and for H₂O, the RMS of the distribution lies within 1σ of the fit, hence the observed scatter is consistent with the stochastic error. For CO inside 1.5 AU the observed RMS dominates the stochastic error (see Table IV). This could be related to nonuniform structure in the distributed component, for example, CO-enriched jets superimposed on a more diffuse background of CO emission (see text).

TABLE IV
Variability of CO Water Production in Comet Hale-Bopp^a

Species ^a	N ^b	σ_s^c	σ_v^d	σ_v/σ_s^e
Native CO alone ($R_h > 2$ AU)	5	0.168	0.108	0.643
H ₂ O	10	0.077	0.066	0.857
Total CO ($R_h < 2$ AU)	7	0.053	0.092	1.713
Distributed CO	7	0.112	0.169	1.510

^a The derived production rate for each species on each date has been divided by Q_{fit} taken from its heliocentric power law fit, to reveal *relative* variability. “Native CO alone” refers to that observed outside $R_h = 2$ AU, for which our observations indicate that the distributed source was not active. Values for H₂O were calculated from production rates (and associated 1σ uncertainties) in Dello Russo *et al.* 2000. “Total CO” refers to combined native and distributed sources within 2 AU of the Sun. “Distributed CO” pertains to the difference between Q_{CO} and the “native” fit extrapolated to $R_h < 2$ AU, as discussed in the text.

^b Number of dates on which the species was observed.

^c Root-mean-square deviation of relative production rates about the corresponding heliocentric power law fit, based on the magnitude of the error bars in Fig. 8 (which approximate associated 1σ stochastic errors): $[\sigma_s \equiv (\sum \sigma_i^2)^{1/2}]$.

^d Root-mean-square deviation of relative production rates about the corresponding heliocentric power law fit, based on the actual variance of each point weighted by its errors:

$$[\sigma_v \equiv (N/(N-1))^{1/2} (\sum (Q_{\text{rel},i} - Q_{\text{rel,mean}})^2 / \sigma_i^2)^{1/2} / (\sum 1/\sigma_i^2)^{1/2}].$$

^e Measure of the actual scatter of each distribution, relative to that predicted solely from the error bars. $\sigma_v/\sigma_s < 1$ indicates that the mean RMS scatter lies within 1σ of the fit; this is the case for water and native CO. For CO within $R_h < 2$ AU, the mean scatter lies outside 1σ of the fit. This could result from nonuniform structure of the distributed component, for example CO-enriched jets in the coma (see text for further discussion).

in the nucleus of Comet Hale-Bopp with the CO mixing ratio observed for ices in star-forming regions can provide information regarding the processing history of the precometary ices. Our derived value of $Q_{\text{Nat}}/Q_{\text{H}_2\text{O}}$ (0.12) places it within the intermediate region (zone II) in Fig. 7 of Chiar *et al.* 1998. Our value is comparable to the mixing ratio of (nonpolar) CO ice found in the envelopes of low-mass protostellar sources such as L1489 IRS and Elias 18, whose $4.7 \mu\text{m}$ absorption spectra have been fitted with ratios of nonpolar CO/polar CO ~ 2.6 and 1.5, respectively (Chiar *et al.* 1998). Our derived $Q_{\text{Nat}}/Q_{\text{H}_2\text{O}}$ is substantially higher than values observed close to young stars (for which little or no CO is typically seen), but is slightly lower than that observed in more quiescent cloud regions (e.g., toward the background field stars El 16 or CK 2), for which nonpolar CO/H₂O ~ 0.2 – 0.6 . Our results therefore suggest that the precometary ices which were incorporated into the nucleus of Hale-Bopp were relatively unprocessed in the solar nebula; however, some depletion of CO during their evolution from the natal interstellar dense cloud core cannot be ruled out.

If the onset of distributed CO emission were related to increased dust release as the comet approached perihelion, a sharp increase similar to that observed for Q_{CO} between 2.0 and 1.5 AU would be expected for the dust. While Q_{CO} follows two distinct distributions, one for $R_h < 2$ AU and one for $R_h > 2$ AU, Q_{dust} appears to fit a single distribution with no such jump near (or inside)

2 AU (Fig. 8). The production of mm-sized dust likewise is characterized by a single distribution (Jewitt and Matthews 1999).

Thus, the onset of distributed CO emission cannot be explained by increased dust production alone. Rather, it is plausible that a threshold (most likely thermal) is reached for release of the species giving rise to additional CO in the coma. We note that the same power law dependence ($\sim R_h^{-1.7}$) exhibited by Q_{CO} for both $R_h < 2$ AU and $R_h > 2$ AU suggests that release of the “parent” giving rise to distributed CO is controlled by sublimation of the same nuclear ice that controls release of native CO and water over the range in heliocentric distance covered by our observations. Note that this similarity in heliocentric behavior does not preclude the existence of one or more vents enriched in CO or in CO-containing material (such as CHON grains). Sublimation of such CO-rich pockets may be responsible for the complex morphology observed in our long-slit profiles of CO emission in Comet Hale-Bopp (see below).

Our results differ from those obtained at millimeter wavelengths in which CO production showed little change between $R_h \sim 3$ AU and 1.6 AU preperihelion but resumed a steep increase ($\sim R_h^{-4.5}$) for $R_h < 1.6$ AU (Biver *et al.* 1997). Biver *et al.* attributed this behavior to CO sublimation from decreased depths in the nucleus following the onset of direct H₂O sublimation. While this may be a contributing effect, our spatially resolved observations demonstrate that accelerated production of the native component cannot totally explain the increase (nearly 4-fold) in Q_{CO} we observe between 2.02 and 1.49 AU preperihelion. Production from a distributed source is clearly evident, and appears to rival production of native CO within $R_h \sim 1.5$ AU.

Compared with native ices, the apparent production of dust changes more rapidly with heliocentric distance (Fig. 8) but this actually reflects the changing grain surface area. Our continuum measurements (and those of Wooden *et al.* 1999) are sensitive to a population of grains having sizes ~ 1 – $10 \mu\text{m}$. If volatile and refractory components are mixed uniformly in the nucleus, the steeper power law exhibited for production of μm -sized dust ($R_h^{-3.6}$; Fig. 8) compared with the production of mm-sized particles ($R_h^{-1.7}$; Jewitt and Matthews 1999) most likely results from increasing dust grain fragmentation with decreasing heliocentric distance. Icy “glue” vaporized at higher dust temperatures could cause higher apparent dust production by virtue of increased radiating surface area after grain fragmentation. Distributed CO could be produced (released) during the fragmentation process; however, we see no obvious correlation between regions of the coma exhibiting enhanced CO emission, and regions of higher continuum intensity (see below), either in our images through the CVF near $2.2 \mu\text{m}$ (Fig. 1) and $3.5 \mu\text{m}$, or in the $4.7\text{-}\mu\text{m}$ continuum sampled in our CO spectral observations.

The higher variability we observe in Q_{Distr} (relative to Q_{H_2O} or Q_{Nat} ; see above), coupled with the observed complex (and variable) structure of our CO profiles, suggests possible contributions from a relatively isotropic native source and one or more sources which appear to be directed (focused) to some extent. For example, these “focused” contributions could originate from

pockets of CO-enriched material (e.g., CHON grains) released from distinct regions of the nucleus. The degree of focusing establishes the resulting morphology, ranging for example from “jets” to a more fanned out distribution of CO in the coma. Interferometric observations of the CO (2-1) rotational line on UT 1997 March 11 ($R_h = 0.99$ AU preperihelion) show evidence for rotating CO jets (Wink *et al.* 1999; Henry *et al.* 2000).

Our CO data consistently reveal the presence of both native and distributed CO emission within 1.5 AU of the Sun, with the peak CO column density frequently displaced from that of the thermal continuum (cf. Figs. 6B–6D). The complex nature of our CO profiles may result from jets superimposed on a more symmetric (although extended) profile (see, e.g., Fig. 6D), and the enhanced scatter in Q_{Distr} could result, at least in part, from CO-enriched jets intersecting our slit.

Both the intensity and direction of the asymmetric outflow should be linked to the rotation of Comet Hale-Bopp. Modeling of our observations must therefore include asymmetric outflow in the coma (e.g., Xie and Mumma 1996b) in addition to symmetric outflow, and must incorporate both photochemistry and cometocentric variations in gas velocity and temperature (Bockelée-Morvan and Crovisier 1987, Boice *et al.* 1990, Xie and Mumma 1996a, Combi 1996).

It is possible that all distributed CO originates in CHON-rich regions of the nucleus. Any volatiles released from CHON grains should initially follow a directed outward flow, and those released closer to the nucleus would be more efficiently isotropized into the diffuse coma by virtue of higher gas densities and therefore higher collision rates. CO released within our typical PSF of 1–2 arcsec ($\sim 1,000$ – $2,000$ km near closest approach to Earth) would be indistinguishable from the native CO source. However, CO released from grains at large cometocentric distances could more easily retain a directed flow and could produce the superimposed structure seen in our CO profiles.

The relatively abrupt onset of the distributed CO source is consistent with a thermal threshold for destruction of such grains in the coma. If the CHON-grain temperature follows that of the μm -sized grains responsible for the continuum flux we observe, the destruction threshold temperature would lie in the range 280–325 K. Super-heating of submicron-sized grains (e.g., to $T_{\text{grain}} \sim 500$ K or higher; Greenberg and d’Hendecourt 1985) was proposed to explain the observed onset (and cessation) of C₂ production near $R_h = 2$ AU in some (although not the majority of) comets (Combi and Fink 1997). A similar phenomenon could be responsible for release of distributed CO (or its progenitor) in Comet Hale-Bopp.

We expect production rates derived from large beam observations to agree with our results for total CO production. The total CO abundance reported by Bockelée-Morvan *et al.* 2000 (23% relative to H₂O) is consistent with our result for total Q_{CO} within 1.5 AU of the Sun ($24 \pm 1\%$). However, our results show that only one-half ($\sim 51\%$) of the total CO is contained as ice in the nucleus, the remainder being produced as a distributed source in the coma.

What is the nature of the released material which gives rise to additional CO in the coma? In Comet Halley, most (>95% of all) formaldehyde was produced from an extended source, and the total production rate of formaldehyde was $\sim 7.5\%$ relative to water, comparable to the amount of CO produced from a distributed source (see Eberhardt 1999 and references therein). Thus, monomeric formaldehyde could account for all of the distributed CO in Comet Halley.

Monomeric formaldehyde (H_2CO) has a photo-dissociation lifetime of $\sim 5 \times 10^3$ s at 1 AU (Huebner *et al.* 1992), or a scale-length of $\sim 5,500$ km (for 1.1 km s^{-1} outflow velocity). Our Q-curves for CO near $R_h = 1$ AU reach their terminal values near this projected distance from the nucleus (see above). Interferometric maps of Comet Hale-Bopp indicate that at least 94% of all H_2CO is produced in the coma (Wink *et al.* 1999). If H_2CO were the precursor to extended CO in Comet Hale-Bopp, then an abundance $\text{H}_2\text{CO}/\text{H}_2\text{O} \sim 12\%$ would be required, somewhat higher than in Comet Halley. However, the relative abundance of H_2CO in Hale-Bopp near 1 AU from the Sun was only $\sim 1.1\%$ relative to water (Biver *et al.* 1997, 1999b; Bockelée-Morvan *et al.* 2000), which is an order of magnitude smaller than our production rate for distributed CO. This H_2CO abundance is based on flux contained within a beam of radius 10,000–20,000 km, similar to the range covered by our slit, and assumes production from a distributed source (Bockelée-Morvan *et al.* 2000). The relative abundance would be even smaller were formaldehyde released as a native source at the nucleus. Thus, it appears that formaldehyde can be at most a very minor source of distributed CO in Hale-Bopp.

It would be interesting to compare the amount of distributed CO contained in regions of enhanced (nonisotropic) emission with $Q_{\text{H}_2\text{CO}}$; however, this is beyond the scope of the present paper. It would also be interesting to search for possible correlations between regions of enhanced CO emission revealed by our observations, and observed CN or C_2 emission arising from jets (Lederer 2000, Lederer *et al.* 2000). In Comet Halley, approximately one-half of the CN was concentrated in jets, the other half resulting from photodissociation of one or more parent species (Klavetter and A'Hearn 1994, A'Hearn *et al.* 1986). However, the jets of CN were not correlated with the jets of small dust grains seen at visible wavelengths, similar to our observed lack of a correlation between the morphology of CO and μm -sized dust in the coma of Comet Hale-Bopp. A comparison of distributed CO with CN in Hale-Bopp could reveal whether both are produced from a common source, such as CHON grains.

SUMMARY

Our long-slit spectroscopic observations of CO emission in Comet Hale-Bopp have permitted a detailed study of line-by-line excitation in the coma at high angular resolution. Within $R_h \sim 1.5$ AU, our results support a dual-source nature for CO production, similar to that seen in Comet Halley during the Giotto spacecraft encounter. We infer a total (native plus dis-

tributed) CO production rate of $24 \pm 1\%$ relative to water, with approximately half of the observed CO contained in the nuclear ice, and half produced in the coma. The abundance of native CO ice ($Q_{\text{Nat}}/Q_{\text{H}_2\text{O}} = 12.4 \pm 0.4\%$) is consistent with that observed in some embedded low-mass protostellar objects. This suggests relatively little processing of the constituent ices prior to incorporation into Comet Hale-Bopp; however, the broad range in CO: H_2O observed in quiescent clouds (~ 0.2 – 0.6) prevents firm conclusions to be drawn in this regard.

In comet Halley, the production rates of native and distributed CO were 3.5% and 7.5% respectively, perhaps suggesting somewhat greater processing of its precometary ices. We stress that, within 1.5 AU of the Sun, we do not directly measure the amount of native CO in Comet Hale-Bopp. Our inferred values for Q_{Nat} within 1.5 AU are based on an extrapolation of (native) CO production rates at $R_h > 2$ AU to smaller distances. We feel this interpretation is valid, based on the similar heliocentric dependence exhibited for production of native CO, water, ethane and mm-sized dust particles. Furthermore, when our Q-curves for CO and H_2O at 1.49 AU pre-perihelion are corrected for attenuation of the solar pump along the line of sight, these support our claim of approximately equal contributions from native and distributed sources of CO. Further refinements must await a detailed investigation of our CO profiles on other dates of observation, including acceleration of and asymmetries in the outflow.

Comparison of relative CO line intensities has allowed a measure of the rotational temperature distribution in the coma. We see an increase in T_{rot} with increasing line-of-sight distance from the nucleus, and this is most pronounced near perihelion (within $R_h \sim 1.1$ AU). We attribute this to photolytic heating of the ambient gas by fast H-atoms and/or by electrons in the coma (both of which are produced primarily by photo-destruction of H_2O). We observe a similar effect for HCN in Hale-Bopp (Magee-Sauer *et al.* 1999), and this may indicate a prominent role for collisions by electrons in maintaining rotational populations in the coma. However, the temperature profile for CO varies from day to day. For example, the gradient of T_{rot} versus ρ is very pronounced on some dates (e.g., April 09.9, Fig. 5E), while at times the profile is quite flat (e.g., February 24, Fig. 5C). This is not yet understood.

The onset of distributed CO production occurred between $R_h = 2.02$ (11 December 1996) and 1.49 AU (21 January 1997) preperihelion. Two lines of evidence support this conclusion: (i) Within $R_h = 1.5$ AU, our CO spatial profiles were consistently very broad compared with those of native volatiles and the continuum, retaining considerable intensity in the far wings near the ends of the slit. This was not seen on dates for which $R_h > 2$ AU. (ii) The total CO production rate increased sharply between 2.0 and 1.5 AU preperihelion. The production rate growth curves for CO inside 1.5 AU reached their terminal values relatively far from the nucleus compared with those for CO outside 2 AU from the Sun, or compared with those for volatiles having a purely native origin (e.g., H_2O , HCN, or C_2H_6). This is true even after correcting our Q-curves for opacity effects. Also, these

terminal values for CO within 1.5 AU were well above those for (scaled) Q-curves of dust or native volatiles. Once active, distributed CO emission was consistently present at all smaller heliocentric distances observed. Postperihelion, the distributed source was still active at $R_h = 1.06$ AU, but was inactive at 2.24 AU and 2.83 AU. Closure of the IRTF for approximately three months (May through July 1997) prevented determination of the heliocentric distance at which the distributed source became inactive.

The relatively abrupt onset of CO production in the coma suggests a thermal threshold rather than a photochemical phenomenon to explain its initiation. The enhanced CO production and more extended spatial distribution were not accompanied by an abrupt change in production of either large (mm-sized) or small ($\sim 1\text{--}10\ \mu\text{m}$ -sized) dust particles, as might occur had a second vent become activated. The abrupt onset of distributed CO suggests that release of its source molecule(s) from smaller grains (e.g., CHON particles) heated above some threshold temperature may be important. Comparison with grain models suggests a threshold temperature of ~ 500 K (Greenberg and d'Hendecourt 1985). Monomeric formaldehyde can contribute at most a minor fraction of distributed CO in Comet Hale-Bopp.

Once it began, production of CO from the precursor proceeded with constant efficiency. Based on the analysis presented in this paper, the ratio of native to distributed CO remained approximately constant. This suggests that the mixing ratio of the precursor species (in the nucleus) was uniform relative to water, and that production of distributed CO was likely dominated by a diffuse source in the coma (whether or not it originated in jets). Within $R_h = 1.5$ AU, CO production exhibited larger variance than can be explained by stochastic noise alone ($Q_{\text{H}_2\text{O}}$ did not show a similar increase). This difference may be linked to the structurally complex and variable nature observed for the spatial profiles of CO. It could be indicative of CO-enriched jets superimposed on a more uniform background of CO production in the coma.

The measurement of spatially resolved rotational temperatures and production rates for cometary volatiles represents a powerful tool for detailed studies of the coma. The free spectral range of CSHELL is such that two CO lines are encompassed per grating setting, hence the rotational population distribution can be sampled with a few judiciously chosen settings. However, this occurs at the expense of temporal resolution, since time is required to re-tune the grating and this affects the results obtained in the case of rapid activity variations. This is especially true when the various CO settings required are interspersed with settings which sample other parent volatiles.

Excitation studies in cometary comae can be improved with the use of cross-dispersed echelle spectrometers incorporating large format (1024×1024 -pixel) InSb detectors. The prototype of this new-generation instrumentation is NIRSPEC, a recently commissioned facility spectrometer at the Keck II 10-meter telescope (McLean *et al.* 1998, McLean 2000). This instrument per-

mits characterization of the rotational distribution of molecular band systems in a single exposure. In 1999, NIRSPEC was used to observe Comet C/1999 H1 (Lee), and eight lines (P3 through R4) of CO were encompassed simultaneously in a single order, as were sixteen lines (P9 through R6) of HCN in a second order (Mumma *et al.* 2001). Such instrumentation will be used for studies of production rates and related time-varying phenomena in future active comets.

APPENDIX: CO OPTICAL DEPTH

Our analysis indicates that approximately equal amounts of CO arose from native and distributed sources (within $R_h = 1.5$ AU), and the scale for the latter source was $\sim 5000\text{--}7000$ km. We now ask whether optical depth effects could affect the apparent shapes of our Q-curves for CO within 1.5 AU of the Sun, particularly for lines-of-sight close to the nucleus.

First, we note that the line-center optical depths are comparable for the pumping transitions of H_2O and CO lines used in our work. However, only the Q-curve for CO shows the gradual rise indicative of a distributed source. The Q-curve for water rises quickly to its terminal value, like that of dust (which is known to be optically thin). The data themselves therefore demonstrate that optical depth effects are not likely to account for the strong difference in behavior exhibited by the Q-curves for water and CO.

Next, we explicitly consider opacity effects in the coma of Comet Hale-Bopp. If CO lines do become optically thick in the inner coma, the corresponding points on the Q-curve could fall below the (true) values they would exhibit under optically thin conditions, and this could in principle mimic the presence of a distributed source. A general treatment must address opacity effects for the solar pump photons and for the emitted photons separately. Here, we show that the latter effect is entirely negligible, and that the former effect introduces (at most) a small correction to the retrieved production rates. We demonstrate that optical depth effects do not significantly influence our retrieved global production rates, nor our conclusion regarding the presence of a significant distributed source for CO.

We consider first the fate of emitted photons. Although emitted CO quanta are subject to scattering in the coma, they are not thermalized during this process (i.e., converted to heat). CO in the coma resides almost entirely in the lowest vibrational level ($v'' = 0$), and its rotational distribution is well characterized by a rotational temperature (see text). If excited to $v' = 1$, radiative decay dominates collisional de-excitation (quenching) everywhere beyond ~ 1 km from the nucleus (Weaver and Mumma 1984), i.e., emitted 1-0 band quanta may be successively scattered, but they are not lost. Scattering can cause a transfer of intensity from the P- to the R-branch, as discussed in the text. However, quanta radiated in transitions from a given excited level ($v' = 1, J'$) to lower levels ($v'' = 0, J'' = J' \pm 1$) can only re-excite the same upper level, if scattered by ambient CO. The escape-to-space probabilities may differ for the two lines emitted from a given upper level, permitting relatively more of the emitted flux to emerge in the R-versus the P-branch lines. However, the summed intensity of P- and R-branch lines originating from a given rotational level in $v' = 1$ still provides a reliable measure of the upper state population (compare the mean of the line pairs R0/P2 and R1/P3 in Fig. A1). The redistribution of intensity should decrease rapidly with increasing J' , because the lower state populations and the respective absorption line strengths become more nearly equal. Hence, optical depth effects on the emitted quanta do not affect our conclusions adversely.

The significance of scattering optical depth may be assessed empirically by comparing the total column densities (N_1) of CO molecules in $v' = 1$, retrieved from individual line fluxes at various offset distances from the nucleus (Fig. A1; see also Eq. (1b), and footnote 5). In the absence of optical trapping, all lines should yield consistent values for N_1 . For beams passing close to the nucleus (left-most panels of Fig. A1), the ratio of P2 to R0 line intensities is lower than the value of 2 (i.e., $(J' + 1)/J'$) predicted for optically thin escape-to-space conditions, implying non-negligible opacity (scattering) along these lines-of-sight. For beams well removed from the nucleus (e.g., those shown in the

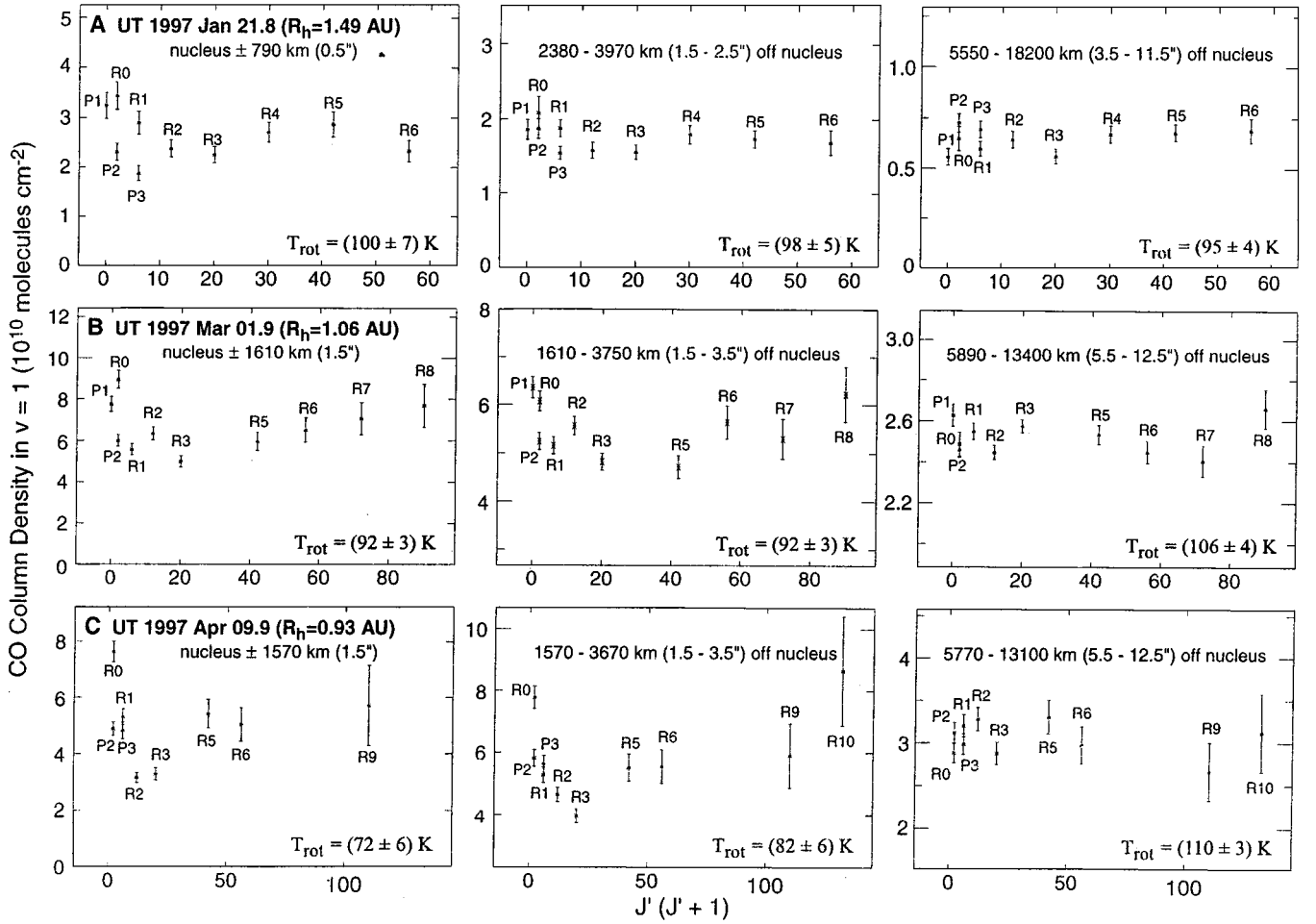


FIG. A1. Column densities of CO molecules in the first excited vibrational state ($v = v' = 1$), as calculated from our (transmittance-corrected) line fluxes on two preperihelion dates and one postperihelion date, using Eq. (1b) (see also footnotes 5 and 7). In each panel, line fluxes have been included over the range of projected distances from the nucleus (i.e., the range of ρ -values) indicated, and averaged east and west of the nucleus. For each date, predicted values near the nucleus are lower for inherently stronger lines. Particularly noticeable is the transfer of intensity from P2 to R0 (and, to a lesser extent, from P3 to R1), resulting from their different optical depths (Table A1). This trend decreases with increasing distance from the nucleus (left to right for each date). In the right-hand panels, which correspond to regions of the coma over which our CO production rates were determined, a common value for N_1 is obtained for all lines (within error), thereby demonstrating that our derived Q_{CO} values are insensitive to opacity effects. Steady-state models for cometary CO (e.g., Chin and Weaver 1984) predict a fractional population of $\sim 7.8 \times 10^{-6} R_h^{-2}$ in the $v' = 1$ state for $T_{\text{rot}} \approx 100$ K, in agreement with our results (compare these values for N_1 with our measured total CO column densities, Fig. 6). Fig. A1 provides only an empirical estimate of relative (line-by-line) CO optical depth effects.

right-hand panels of Fig. A1), line intensities emitted from a common level J' are in their statistical ratio (within 1σ) and the retrieved values of N_1 agree within stochastic errors, even for the line pairs (P2, R0) and (P3, R1), demonstrating that optical depth effects are small for these lines-of-sight.

We next evaluate optical depth effects experienced by the solar pump. For a coma characterized by spherically symmetric uniform outflow, the CO column density (N_0 , molecules cm^{-2}) along a radius vector from the nucleus is given by

$$N_0 = \frac{Q_{\text{CO}}}{4\pi V_o} \int_{R_0}^{\infty} dR \frac{\exp(-R\Lambda)}{R^2}, \quad (\text{A1})$$

where V_o is the gas outflow speed (taken to be $1.1 \times 10^5 R_h^{-0.5} \text{ cm s}^{-1}$), and Λ (cm) is the photo-dissociation scale length for CO. Using standard

recurrence relations (Abramovitz and Stegun 1964), Eq. (A2) becomes

$$N_0 = \frac{Q_{\text{CO}}}{4\pi V_o R_0} \left\{ \exp(-\alpha R_0) - \alpha R_0 \left[-\gamma - \ln(\alpha R_0) + \sum_{n=1}^{\infty} a_n (\alpha R_0)^n \right] \right\}, \quad (\text{A2})$$

which is valid over the range $0 \leq \alpha R_0 \leq 1$. In Eq. (A2), $\alpha = 1/\Lambda$, $\gamma = 0.57721$, and the coefficients a_n are less than unity and decrease rapidly with increasing index n .

For a stationary velocity distribution, the corresponding optical depth is $\tau_\nu = K_\nu N_0$, where K_ν ($\text{cm}^2 \text{ molecule}^{-1}$) is the absorption coefficient at frequency ν . For Doppler-broadened lines at line center, $K_0 = (\ln 2/\pi)^{1/2} S_{\text{line}}(T)/\Delta\nu_D$, where $S_{\text{line}}(T)$ is the line strength (cm molecule^{-1}) at rotational temperature T , and $\Delta\nu_D$ (cm^{-1}) is the Doppler line width ($\Delta\nu_D \cong 3.58 \times 10^{-7} \nu_0 [T/M]^{1/2}$) (Pugh and Rao 1976). Here, ν_0 (cm^{-1}) is the line-center (rest) frequency and

M is the molecular weight of the absorbing gas molecules ($=28 \text{ g mole}^{-1}$ for CO). (In the expression for $\Delta\nu_D$, T represents the kinetic temperature, and this should be approximately equal to T_{rot} in the inner coma.)

The line strength can be expressed in terms of the total band strength (S_{band}) as $S_{\text{line}}(T) = S_{\text{band}}(T) f_{0,J''}(T) \epsilon_J$, where $f_{0,J''}(T)$ represents the fraction of all CO molecules in the lower ro-vibrational state at (rotational) temperature T . The Hönl–London factors for absorption (ϵ_J) are expressed in terms of upper state rotational quantum number as $J'/(2J'-1)$ for R-branch lines, and as $(J'+1)/(2J'+3)$ for P-branch lines (Herzberg 1950). For the $v=1-0$ band of CO, we adopt $S_{\text{band}} = 9.80 \times 10^{-18} \text{ cm molecule}^{-1}$ (Pugh and Rao 1976). Thus, the absorption coefficient at line center becomes

$$K_0(\text{cm}^2\text{molecule}^{-1}) = 6.81 \times 10^{-11}(T)^{-1/2} \epsilon_J f_{0,J''}(T)/\nu_0. \quad (\text{A3})$$

For our treatment of optical depth, it is convenient to define a critical distance (R_c) from the nucleus at which the optical depth of a given CO line reaches unity at line center ($\tau_0 = 1$), along a radius vector from the Sun to R_c (see Mumma and DiSanti (in preparation) for a complete discussion). The corresponding critical column density is given by $N_{\text{crit}} = K_0^{-1}$. Eq. (A2) can be solved explicitly for R_c , but the quantity in curly brackets is essentially unity for a long-lived species such as CO ($\alpha R_c \ll 1$), and so

$$N_{\text{crit}} \cong (Q_{\text{CO}}/4\pi V_0 R_c) = K_0^{-1}, \quad (\text{A4})$$

or,

$$R_c(\text{km}) \sim (10^{-5} Q_{\text{CO}} K_0 / 4\pi V_0) \sim 4.92 \times 10^{-22} Q_{\text{CO}} (T/R_h)^{-1/2} \epsilon_J f_{0,J''}(T) / \nu_0. \quad (\text{A5})$$

In Table AI, we list values of R_c for several lines, based on our total measured (global) production rates for CO ($Q_{\text{CO}} = 10.7$ and 20.7×10^{29} molecules s^{-1} at $R_h = 1.5$ and 1.0 AU, respectively; cf. Table III and Fig. 8). We use the total

TABLE AI

CO Line Center Optical Depth Estimates for Comet Hale-Bopp

CO line	J'	ν (cm^{-1}) ^a	ϵ_J	$f_{0,J''}$ (100 K)	K_0 ^b	N_{crit} ^c	R_c^d (km) ($R_h = 1.5$)	R_c^d (km) ($R_h = 1.0$)
P1	0	2139.427	0.333	0.078	.827	12.09	773	1240
P2	1	2135.547	0.400	0.116	1.48	6.76	1390	2220
P3	2	2131.632	0.429	0.138	1.89	5.29	1770	2830
P4	3	2127.683	0.444	0.142	2.02	4.95	1890	3020
P5	4	2123.699	0.455	0.131	1.91	5.24	1790	2860
R0	1	2147.082	1.000	0.027	.856	11.68	801	1280
R1	2	2150.856	0.667	0.078	1.65	6.06	1540	2470
R2	3	2154.596	0.600	0.116	2.20	4.55	2060	3290
R3	4	2158.300	0.571	0.138	2.49	4.01	2330	3730
R4	5	2161.969	0.556	0.142	2.49	4.02	2330	3730
R5	6	2165.602	0.545	0.131	2.25	4.44	2100	3370
R6	7	2169.198	0.538	0.112	1.89	5.29	1770	2830
R7	8	2172.759	0.533	0.087	1.45	6.90	1360	2171
R8	9	2176.284	0.529	0.064	1.06	9.43	988	1590
R9	10	2179.772	0.526	0.043	.707	14.14	662	1060
R10	11	2183.224	0.524	0.028	.458	21.83	428	686

^a Rest frequency in wavenumbers.

^b Absorption coefficient at line center for a rotational of 100 K ($10^{-16} \text{ cm}^2 \text{ molecule}^{-1}$).

^c CO column density at which optical depth unity at line center is reached ($10^{15} \text{ molecules cm}^{-2}$).

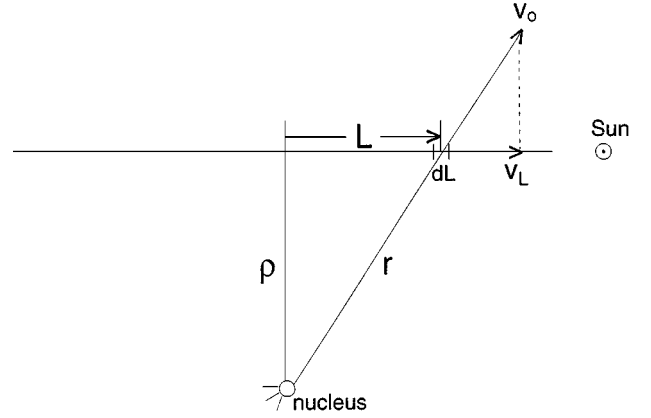


FIG. A2. Schematic depicting the geometrical parameters we use in our optical depth calculations. In our simplified model, the outflow velocity V_0 is assumed to have a uniform magnitude regardless of position in the coma, and this overestimates the effects of optical depth compared with the more realistic case of acceleration in the outflow. The correction to our measured CO column density depends critically upon the ratio of the projected distance ρ to the critical distance R_c . Our model permits evaluation of the opacity in the incident solar pump contributed by a given parcel of gas lying a distance r from the nucleus. See text for details.

CO production rate (Q_{CO}) rather than the native Q alone, so as to overestimate the effects of optical depth.

The column density integrated (entirely through the coma) along a line-of-sight offset by distance ρ from the nucleus is given by

$$N(\rho) = Q_{\text{CO}}/4V_0\rho. \quad (\text{A6})$$

Comparison with Eq. (A4) demonstrates that $N(\rho) = N_c[\pi R_c/\rho]$, hence the line-center optical depth along the offset tangent path is $[\pi R_c/\rho]$. For $\rho = R_c$, the optical depth (through the coma) would be π (or, $\pi/2$ at the tangent point).

The effective g-factor at $\rho = R_c$ would be severely reduced from the optically thin value, were the coma characterized by a stationary velocity distribution. However, the optical depth experienced by the solar pump is greatly reduced when the effect of outflow is included. Projection of outflow velocities along the line-of-sight in the coma leads to reduced “shadowing” of molecules and hence to reduced opacity in the CO lines. This can be appreciated by recognizing that a differential velocity of only $\sim 200 \text{ m s}^{-1}$ is sufficient to reduce the effective absorption coefficient by two-fold (i.e., to $K_0/2$, and this speed is approximately equal to the Doppler velocity dispersion for CO at 100 K. (Emitted CO quanta experience a similar reduction in the scattering optical depth.)

Mumma and DiSanti (in preparation) developed a method for estimating reduced g-factors, including the effects of velocity projection. Their model includes the dispersion in outflow velocity as a function of location in the coma, but it ignores acceleration of the outflowing gas. This simplifies the formalism but it overestimates the effects of optical depth. True column densities are obtained by correcting the apparent column densities derived from the measured line intensities using optically thin g-factors. Here, we follow their method for calculating the attenuation of the solar pump, and we use it to correct our measured Q-curves for water and CO on UT 1997 January 21.

It is convenient to parameterize the problem as depicted in Fig. A2. The variable L represents the distance from the tangency point along a line toward the Sun, r is the distance from the nucleus to a given point in the coma, and V_L is the component of outflow velocity projected along the line-of-sight. The contribution to the optical depth (at frequency ν) from CO along the path between L and $L + dL$ is $d\tau_\nu(L) = K_\nu(L)n(L)dL$, where $n(L)$ is the (total)

number density of CO molecules (cm^{-3}) between L and $L + dL$, and $K_\nu(L)$ is the line absorption coefficient at frequency ν over this same region. Integration along the entire path is most easily done in velocity space:

$$\tau_\nu = \frac{R_c}{\rho} \int_{-v_0}^{v_0} \frac{\exp\left\{\frac{-\ln(2)}{\Delta v_D} \left[\nu - v_0 \left(1 - \frac{V_L}{c}\right)\right]^2\right\}}{\sqrt{V_0^2 - V_L^2}} \times \exp\left\{\frac{-\rho}{R_c} \frac{V_0 R_c}{\Delta \sqrt{V_0^2 - V_L^2}}\right\} dV_L. \quad (\text{A7})$$

This is more conveniently evaluated as a summation,

$$\tau_\nu = \Delta V_L \frac{R_c}{\rho} \left[\sum_{-V_0}^{+V_0} f_{V_L, \nu} \right], \quad (\text{A8})$$

where $f_{V_L, \nu}$ represents the integrand in Eq. (A7).

We evaluated τ_ν over the range $V_L = -0.995V_0$, to $+0.995V_0$, for incident solar photon frequencies between $\nu_{\min} = \nu_0(1 - 1.75V_0/c)$ and $\nu_{\max} = \nu_0(1 + 1.75V_0/c)$, and for several values of the ratio ρ/R_c . Results for the spectral absorbance $[1 - \exp(-\tau_\nu)]$ are shown in Fig. A3. The flux removed from the solar continuum along this path is

$$\Delta I = I_0 \int_{\nu_{\min}}^{\nu_{\max}} \{1 - \exp(-\tau_\nu)\} d\nu. \quad (\text{A9})$$

We may write Eq. (A9) in terms of an effective g -factor (g_{eff}) and the true column density (N_{true}), or the optically thin g -factor (g_{thin}) and an apparent column density (N_{app}),

$$\Delta I = g_{\text{eff}} N_{\text{true}} \equiv g_{\text{thin}} N_{\text{app}}, \quad (\text{A10})$$

where $g_{\text{thin}} = I_0 S_{\text{line}}$. The quantity N_{app} is presented in Fig. A1, for example.

We evaluated the integral (A9) as a summation, and we chose the step size in frequency $\Delta\nu (= v_0 \Delta V_L / c)$ to correspond to the velocity bin size ΔV_L (we used $\Delta V_L = 5 \times 10^{-3} V_0$ in our calculations). The limits of integration (ν_{\min} , ν_{\max}) were chosen so as to include all non-negligible values of τ_ν (Fig. A3). The apparent column density (N_{app}) is then

$$N_{\text{app}} = \frac{\left(\sum_{\nu_{\min}}^{\nu_{\max}} [1 - e^{-\tau_\nu}]\right) \Delta\nu}{S_{\text{line}}} \equiv \frac{(\text{SUM1})(\Delta\nu)}{S_{\text{line}}}. \quad (\text{A11})$$

The true column density may be written as

$$N_{\text{true}} = \frac{Q_{\text{CO}}}{4\pi V_0 \rho} \int_{-V_0}^{V_0} \frac{\exp\left\{\frac{-\rho V_0}{\Delta} (V_0^2 - V_L^2)^{-1/2}\right\}}{\sqrt{V_0^2 - V_L^2}} dV_L, \quad (\text{A12})$$

or

$$N_{\text{true}} = \left(\sqrt{\frac{\pi}{\ln 2}} \frac{\Delta v_D R_c}{S_{\text{line}} \rho}\right) (\Delta V_L) \times \left(\sum_{-V_0}^{V_0} \frac{\exp\left\{-\frac{\rho V_0}{\Delta} (V_0^2 - V_L^2)^{-1/2}\right\}}{\sqrt{V_0^2 - V_L^2}}\right) \equiv \left(\sqrt{\frac{\pi}{\ln 2}} \frac{\Delta v_D}{S_{\text{line}}}\right) \frac{R_c}{\rho} (\Delta V_L)(\text{SUM2}). \quad (\text{A13})$$

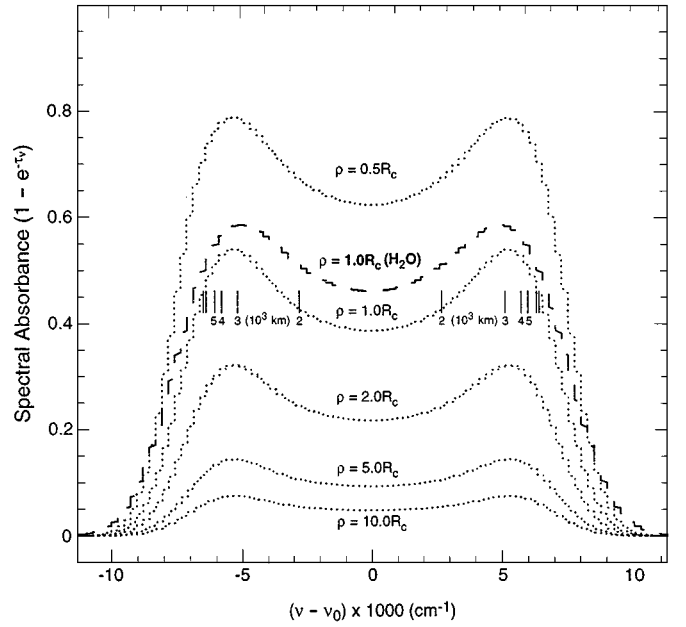


FIG. A3. Spectral absorbance ($1 - e^{-\tau_\nu}$) solutions (from Eq. (A7)), shown here for CO for several values of the ratio ρ/R_c . For comparison, the solution for the water line $\nu_3 - \nu_2 1_{11} - 1_{10}$ with $\rho/R_c = 1.0$ is also shown. The slightly greater spectral width for the H_2O absorbance curve results from its larger Doppler width Δv_D ($3.17 \times 10^{-3} \text{ cm}^{-1}$) compared with that for CO ($\Delta v_D = 1.45 \times 10^{-3} \text{ cm}^{-1}$) (both for $T = 100 \text{ K}$). Each CO molecule absorbs solar continuum photons at a frequency determined by its line-of-sight velocity V_L (relative to the Sun). The abscissa has units of $.001 \text{ cm}^{-1}$, and represents the displacement of absorbed photon frequencies relative to the line-center frequency in the heliocentric rest frame, thus zero corresponds to the tangent point $L = V_L = 0$ in Fig. A2. The ordinate shows the attenuation in the solar pump (i.e., reduction in the g -factor) at frequency $\nu - \nu_0$. Note that the absorbance increases sharply for beams passing close to the nucleus (small values of ρ/R_c). Also shown are vertical tick marks for the CO absorbance plot $\rho/R_c = 1.0$ (i.e., $\rho = 1,800 \text{ km}$). Each tick mark indicates the radial distance from the nucleus (r , in units of 10^3 km ; cf Fig. A2) at which the corresponding line-center frequency shift ($\nu - \nu_0$) occurs. For example, along the beam $\rho = 1.0R_c$, CO molecules located a distance $r \approx 2,840 \text{ km}$ from the nucleus absorb (at line center) solar continuum photons displaced by $\pm 5 \times 10^{-3} \text{ cm}^{-1}$, relative to CO molecules at the tangent point ($r = 1,800 \text{ km}$). The two tick marks farthest from zero displacement (not having numerical labels) correspond to 10^4 and 10^6 km from the nucleus. The non-negligible opacity even at 10^6 km from the nucleus is due to the broad Doppler velocity envelope at 100 K . We expect that including acceleration in the coma will cause τ_ν to drop to zero more quickly beyond $r \sim 10^5 \text{ km}$.

Now the apparent column density (or production rate) can be corrected to the true column density (the true production rate) through a correction factor, F_{corr} , given by the ratio $N_{\text{true}}/N_{\text{app}}$:

$$F_{\text{corr}} \equiv \left(\frac{N_{\text{true}}}{N_{\text{app}}}\right) = \left(\Delta v_D \sqrt{\frac{\pi}{\ln 2}}\right) \frac{R_c}{\rho} \frac{(\Delta V_L)(\text{SUM2})}{(\Delta\nu)(\text{SUM1})}. \quad (\text{A14})$$

Table AII lists, at 1 arc-second intervals, correction factors appropriate to our UT 1997 January 21 observations. For CO we use $R_c = 1800 \text{ km}$, which represents the mean value for all CO lines observed on this date (Table AI). For the comparative water line $\nu_3 - \nu_2 1_{11} - 1_{10}$ at $\nu_0 = 2151.19 \text{ cm}^{-1}$, we calculate $R_c \sim 2500 \text{ km}$. We applied these correction factors to our apparent Q-curves for water and CO (Fig. A4). As in our prior analysis, the (now corrected) Q-curve

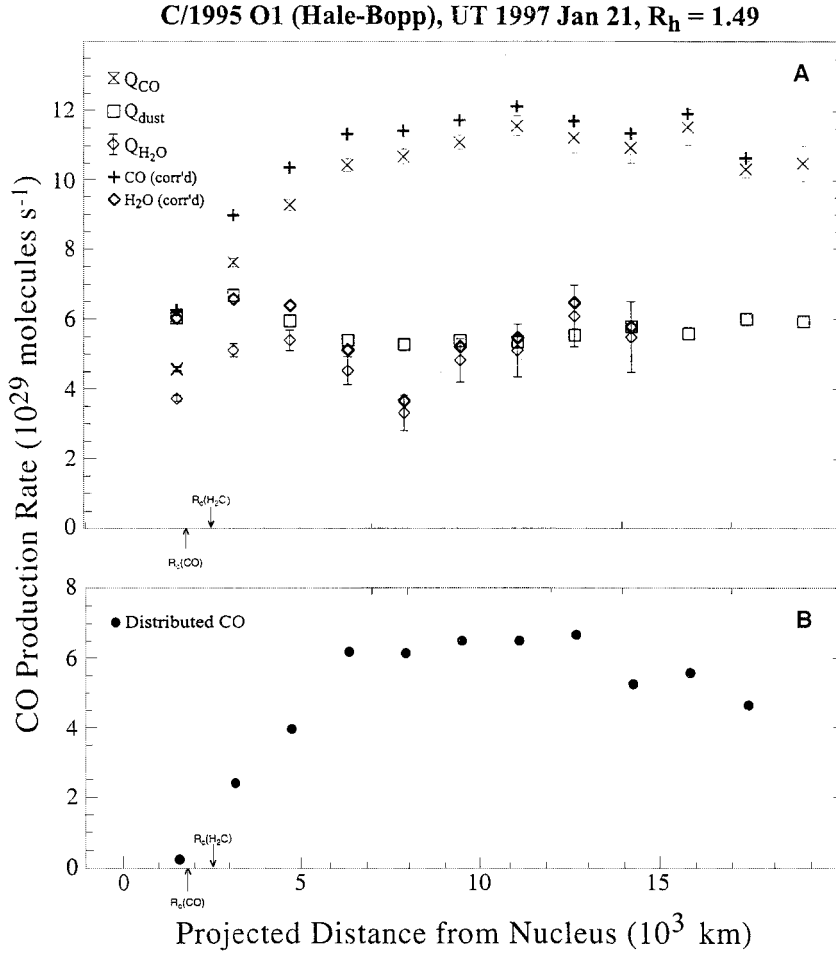


FIG. A4. Q-curves for Comet Hale-Bopp for 1997 January 21, after correcting each for optical depth in the solar pump by the factors (F_{corr}) listed in Table AII. A. Corrected Q-curves for CO (pluses) and H_2O (large, heavy diamonds) lie somewhat above their uncorrected counterparts (compare Fig. 7B), but the ratio of corrected terminal values supports roughly equal contributions of native and distributed CO, as suggested by our previous analysis (DiSanti *et al.* 1999). Q_{dust} is scaled to the corrected water point 1 arc-second off the nucleus. B. The difference between opacity-corrected Q-curves for CO and H_2O , which we take to represent production from the distributed CO component alone. For the point near $\rho = 8 \times 10^3$ km, the continuum point was subtracted from the corrected CO point, and similarly for the two points farthest from the nucleus. This indicates that the distributed source was fully developed by $\rho \approx 6 - 7 \times 10^3$ km from the nucleus, as stated in the text.

TABLE AII

Optical Depth Corrections for CO and H_2O in Comet Hale-Bopp on UT 1997 January 21 ($R_h = 1.49$ AU, $\Delta = 2.20$ AU)

ρ (arc-sec)	ρ (km)	CO ($R_c = 1,800$ km)		H_2O ($R_c = 2,500$ km)	
		ρ/R_c	F_{corr}	ρ/R_c	F_{corr}
1.0	1600	0.822	1.363	0.638	1.619
2.0	3190	1.76	1.170	1.28	1.285
3.0	4790	2.64	1.109	1.92	1.183
4.0	6380	3.53	1.080	2.55	1.133
5.0	7980	4.41	1.062	3.19	1.104
6.0	9570	5.29	1.050	3.83	1.085
7.0	11200	6.17	1.042	4.47	1.072
8.0	12800	7.05	1.036	5.11	1.062
9.0	14400	7.93	1.031	5.74	1.054
10.0	15960	8.82	1.028	6.38	1.048
11.0	17600	9.70	1.024	7.02	1.043

for H_2O is taken to be a proxy of the contribution from native CO and, as before, this is approximately half of the (corrected) total Q_{CO} . Thus our conclusions as to the relative amounts of native and distributed CO in Comet Hale-Bopp remain unchanged, based on our analysis to date. Future work will extend this analysis to other dates of observation, and will include considerations of acceleration and observing geometry.

ACKNOWLEDGMENTS

This work was supported by the NASA Planetary Astronomy Program under grants NAG5-7905 to M. A. DiSanti, and RTOP 344-32-30-07 to M. J. Mumma. We are grateful to the staff of the NASA Infrared Telescope Facility for their outstanding support throughout our Comet Hale-Bopp campaign. We thank T. Rettig and R. Novak for their participation in the observations. MD thanks R. Novak for discussions regarding the excitation formalism, and M. Combi for correspondence regarding gas hydrodynamics in the coma of Comet Hale-Bopp. We thank D. Bockelée-Morvan and an anonymous referee for suggestions which improved the manuscript. The IRTF is operated by the University of Hawaii under contract to NASA.

REFERENCES

- A'Hearn, M. F., and P. D. Feldman 1980. Carbon in Comet Bradfield (1979I). *Astrophys. J.* **242**, L187–L190.
- A'Hearn, M. F., S. Hoban, P. V. Birch, C. Bowers, R. Martin, and D. A. Klinglesmith, III 1986. Cyanogen jets in Comet Halley. *Nature* **327**, 649–652.
- Balsiger, H., K. Altwegg, F. Bühler, J. Geiss, A. G. Ghielmetti, B. E. Goldstein, R. Goldstein, P. Hemmerich, G. Kulzer, A. J. Lazarus, A. Meier, M. Neugebauer, U. Rettenmund, H. Rosenbauer, R. Schwen, E. G. Shelley, E. Ungstrup, and D. Young 1986. The ion composition and dynamics at Comet Halley. *Nature* **321**, 330–335.
- Biver, N., H. Rauer, D. Despois, R. Moreno, G. Paubert, D. Bockelée-Morvan, P. Colom, J. Crovisier, E. Gerard, and L. Jorda 1996. Substantial outgassing of CO from Comet Hale-Bopp at large heliocentric distance. *Nature* **380**, 137–139.
- Biver, N., D. Bockelée-Morvan, P. Colom, J. Crovisier, J. K. Davies, W. R. F. Dent, D. Despois, E. Gerard, E. Lellouch, H. Rauer, R. Moreno, and G. Paubert 1997. Evolution of the outgassing of Comet Hale-Bopp (C/1995 O1) from radio observations. *Science* **275**, 1915–1918.
- Biver, N., D. Bockelée-Morvan, J. Crovisier, J. K. Davies, H. E. Matthews, J. E. Wink, H. Rauer, P. Colom, W. R. F. Dent, D. Despois, R. Moreno, G. Paubert, D. Jewitt, and M. Senay 1999a. Spectroscopic monitoring of Comet C/1996 B2 (Hyakutake) with the JCMT and IRAM radio telescopes. *Astron. J.* **118**, 1850–1872.
- Biver, N., D. Bockelée-Morvan, P. Colom, J. Crovisier, B. Germain, E. Lellouch, J. K. Davies, W. R. F. Dent, R. Moreno, G. Paubert, J. Wink, D. Despois, D. C. Lis, D. Mehringer, D. Benford, M. Gardner, T. G. Phillips, M. Gunnarsson, H. Rickman, A. Winnberg, P. Bergman, L. E. B. Johansson, and H. Rauer 1999b. Long term evolution of the outgassing of Comet Hale-Bopp from radio observations. *Earth, Moon, Planets* **78**, 5–11.
- Bockelée-Morvan 1987. A model for the excitation of water in comets. *Astron. Astrophys.* **281**, 169–181.
- Bockelée-Morvan, D., and J. Crovisier 1987. The role of water in the thermal balance of the coma. In *Symposium on the Diversity and Similarity of Comets*, ESA SP-278, pp. 235–240. Brussels.
- Bockelée-Morvan, D., J. Crovisier, P. Colom, and D. Despois 1994. The rotational lines of methanol in comets Austin 1990 V and Levy 1990 XX. *Astron. Astrophys.* **287**, 647–665.
- Bockelée-Morvan, D., D. C. Lis, J. E. Wink, D. Depois, J. Crovisier, R. Bachiller, D. J. Benford, N. Biver, P. Colom, J. K. Davies, E. Gérard, B. Germain, M. Houde, D. Mehringer, R. Moreno, G. Paubert, T. G. Phillips, and H. Rauer 2000. New molecules found in comet C/1995 O1 (Hale-Bopp). *Astron. Astrophys.* **353**, 1101–1114.
- Boice, D. C., M. J. Sablik, and I. Konno 1990. Distributed coma sources and the CH₄/CO ratio in Comet Halley. *Geophys. Res. Lett.* **17**, 1813–1816.
- Boice, D. C., A. L. Cochran, M. A. DiSanti, and W. F. Huebner 1998. Chemistry in the dusty coma of Comet Hale-Bopp. *BAAS* **30**(3), 1063.
- Boice, D. C., and J.-I. Watanabe 1999. Dust gas flow in the inner coma of Comet Hale-Bopp. *BAAS* **31**(4), 1100.
- Chiar, J. E., A. J. Adamson, T. H. Kerr, and D. C. B. Whittet 1995. High-resolution studies of solid CO in the Taurus dark cloud: characterizing the ices in quiescent clouds. *Astrophys. J.* **455**, 234–243.
- Chiar, J. E., P. A. Gerakines, D. C. B. Whittet, Y. J. Pendleton, A. G. G. M. Tielens, A. J. Adamson, and A. C. A. Boogert 1998. Processing of icy mantles in protostellar envelopes. *Astrophys. J.* **498**, 716–727.
- Chin, G., and H. A. Weaver 1984. Vibrational and rotational excitation of CO in comets. *Astrophys. J.* **285**, 858–869.
- Combes, M., V. I. Moroz, J. Crovisier, T. Encrenaz, J.-P. Bibring, A. V. Gringoriev, N. F. Sanko, N. Coron, J. F. Crifo, R. Gispert, D. Bockelée-Morvan, Yu. V. Nikolsky, V. A. Krasnopolsky, T. Owen, C. Emerich, J. M. Lamarre, and F. Rocard 1988. The 2.5–12 μm spectrum of Comet Halley from the IKS-VEGA experiment. *Icarus* **76**, 404–436.
- Combi, M. R. 1996. Time-dependent gas kinetics in tenuous planetary atmospheres: The cometary coma. *Icarus* **123**, 207–226.
- Combi, M. R., and U. Fink 1997. A critical study of molecular photodissociation and CHON grain sources for cometary C₂. *Astrophys. J.* **484**, 879–890.
- Combi, M. R., K. Kabin, D. L. DeZeeuw, T. I. Gombosi, and K. G. Powell 1999. Dust-gas interrelations in comets: Observations and theory. *Earth, Moon, Planets* **79**, 275–306.
- Crovisier, J. 1987. Rotational and vibrational synthetic spectra of linear parent molecules in comets. *Astron. Astrophys. Supp.* **68**, 223–258.
- Crovisier, J., T. Encrenaz, and M. Combes 1991. Carbon suboxide in comet Halley. *Nature* **353**, 610.
- Crovisier, J., N. Biver, D. Bockelée-Morvan, P. Colom, L. Jorda, E. Lellouch, G. Paubert, and D. Despois 1995. Carbon monoxide outgassing from Comet P/Schwassmann-Wachmann 1. *Icarus* **115**, 213–216.
- Crovisier, J., and T. Encrenaz 2000. *Comet Science: The Study of Remnants from the Birth of the Solar System*, p. 129. Cambridge Univ. Press, Cambridge UK.
- Dello Russo, N., M. A. DiSanti, M. J. Mumma, K. Magee-Sauer, and T. W. Rettig 1998. Carbonyl sulfide in Comets C/1996 B2 (Hyakutake) and C/1995 O1 (Hale-Bopp): Evidence for an extended source in Hale-Bopp. *Icarus* **135**, 377–388.
- Dello Russo, N., M. J. Mumma, M. A. DiSanti, K. Magee-Sauer, R. Novak, and T. W. Rettig 2000. Water production and release in C/1995 O1 Hale-Bopp. *Icarus* **143**, 324–337.
- Dello Russo, N., M. J. Mumma, M. A. DiSanti, and K. Magee-Sauer 2001. Ethane production and release in Comet C/1995 O1 Hale-Bopp, in press.
- DiSanti, M. A., M. J. Mumma, J. H. Lacy, and P. Parmar 1992. A possible detection of infrared emission from carbon monoxide in Comet Austin (1989c1). *Icarus* **96**, 151–160.
- DiSanti, M. A., M. J. Mumma, T. R. Geballe, and J. K. Davies 1995. Systematic observations of methanol and other organics in Comet P/Swift-Tuttle: Discovery of new spectral structure at 3.42 μm . *Icarus* **116**, 1–17.
- DiSanti, M. A., M. J. Mumma, N. Dello Russo, K. Magee-Sauer, R. Novak, and T. W. Rettig 1999. Half the carbon monoxide of comet Hale-Bopp originates in nuclear ices. *Nature* **399**, 662–665.
- Eberhardt, P. et al. 1987. The CO and N₂ abundance in comet P/Halley. *Astron. Astrophys.* **187**, 481–484.
- Eberhardt, P. 1999. Comet Halley's gas composition and extended sources: Results from the neutral mass spectrometer on Giotto. *Space Sci. Rev.* **90**, 45–52.
- Feldman, P. D., and W. H. Brune 1976. Carbon production in comet West 1975n. *Astrophys. J.* **209**, L45–L48.
- Feldman, P. D. 1978. A model of carbon production in a cometary coma. *Astron. Astrophys.* **70**, 547–553.
- Feldman, P. D., M. Festou, P. M. Rodriguez, and R. Gonzales 1996. *IAU Circ.* **6370**.
- Festou, M. C., and P. D. Feldman 1987. Comets. In *Exploring the Universe with the IUE Satellite* (Y. Kondo, Ed.), Astrophysics and Space Science Library Vol. 129, pp. 101–118. Reidel, Dordrecht.
- Festou, M. C. 1990. Comparative cometology from IUE observations. In *Evolution in Astrophysics*, ESA SP-310, pp. 3–10. ESTEC, Noordwijk.
- Green, S. F., J. A. M. McDonnell, G. S. A. Pankiewicz, and J. C. Zarnecki 1986. The UKIRT infrared observational program. In *20th ESLAB Symposium on the Exploration of Halley's Comet, Vol. 2*, ESA SP-250, pp. 81–86.
- Greene, T. P., A. T. Tokunaga, D. W. Toomey, and J. S. Carr 1993. CSHELL: A high spectral resolution 1–5 μm cryogenic echelle spectrograph for the IRTF. *Proc. Spie* **1946**, 311–324.
- Greenberg, J. M., and A. Li 1998. From interstellar dust to comets: the extended CO source in comet Halley. *Astron. Astrophys.* **332**, 374–384.
- Greenberg, J. M., and L. B. d'Hendecourt 1985. Evolution of ices from interstellar space to the solar system. In *Ices in the Solar System* (J. Klinger, D. Benest, A. Dollfus, and R. Smoluchowski, Eds.), pp. 185–204. Reidel, Dordrecht.

- Henry, F., D. Bockelee-Morvan, J. Crovisier, and J. Wink 2000. Radio interferometric observations of rotating CO jets in Comet C/1995 O1 Hale-Bopp. *BAAS* **32**(3), 1073.
- Herzberg, G. 1950. *Spectra of Diatomic Molecules*. Van Nostrand-Reinhold, New York.
- Hoban, S., M. J. Mumma, D. C. Reuter, M. A. DiSanti, and R. R. Joyce 1991. A tentative identification of methanol as the progenitor of the 3.52- μm emission feature in several comets. *Icarus* **93**, 122–134.
- Huebner, W. F. 1987. First polymer in space identified in Comet Halley. *Science* **237**, 628–630.
- Huebner, W. F., D. C. Boice, and C. M. Sharp 1987. Polyoxymethylene in comet Halley. *Astrophys. J.* **320**, L149–L152.
- Huebner, W. F., J. J. Keady, and S. P. Lyon 1992. Solar photo rates for planetary atmospheres and atmospheric pollutants. *Astrophys. Space Sci.* **195**, 1–294.
- Huebner, W. F., H. U. Keller, D. Jewitt, J. Klinger, and R. West (Eds.) 1992. *Workshop on the Activity of Distant Comets*. Southwest Research Inst., San Antonio.
- Huntress, W. T., Jr., M. Allen, and M. Delitsky 1991. Carbon suboxide in comet Halley? *Nature* **352**, 316–318.
- Irvine, W. M., J. E. Dickens, A. J. Lovell, F. P. Schloerb, M. Senay, E. A. Bergin, D. Jewitt, and H. E. Matthews 1998. Chemistry in cometary comae. *Faraday Disc.* **109**, 475–492.
- Irvine, W. M., J. E. Dickens, A. J. Lovell, F. P. Schloerb, M. Senay, E. A. Bergin, D. Jewitt, and H. E. Matthews 1999. The HNC/HCN ratio in comets. *Earth, Moon, Planets* **78**, 29–35.
- Jewitt, D., M. Senay, and H. E. Matthews 1996. Observations of carbon monoxide in Comet Hale-Bopp. *Science* **271**, 1110–1113.
- Jewitt, D., and H. E. Matthews 1999. Particulate mass loss from Comet Hale-Bopp. *Astron. J.* **117**, 1056–1062.
- Kissel, J., D. E. Brownlee, K. Buchler, B. C. Clark, H. Fechtig, E. Grun, K. Hornung, E. B. Igenbergs, E. K. Jessberger, F. R. Krueger, H. Kuczera, J. A. M. McDonnell, G. M. Morfill, J. Rahe, G. H. Schwehm, Z. Sekanina, N. G. Utterback, H. J. Volk, and H. A. Zook 1986. Composition of comet Halley dust particles from Giotto observations. *Nature* **321**, 336–337.
- Klavetter, J. J., and M. F. A'Hearn 1994. An extended source for CN jets in Comet P/Halley. *Icarus* **107**, 322–334.
- Krankowsky, D. 1990. The composition of comets. In *Comets in the Post-Halley Era* (R. L. Newburn, J. Rahe, and M. Neugebauer, Eds.), pp. 855–877. Kluwer Academic, Amsterdam.
- Kunde, V. G., and W. C. Maguire 1974. A direct integration transmittance model. *J. Quant. Spectrosc. Radiat. Transf.* **14**, 803–817.
- Lämmerzahl, P., D. Krankowsky, R. R. Hodges, U. Stubbemann, J. Woweries, I. Herrwerth, J. J. Berthelier, J. M. Illiano, P. Eberhardt, U. Dolder, W. Schulte, and J. H. Hoffman 1987. Expansion velocity and temperatures of gas and ions measured in the coma of comet P/Halley. *Astron. Astrophys.* **187**, 169–173.
- Lang, K. R. 1980. *Astrophysical Formulae*, 2nd. ed. Springer-Verlag, New York. Table 21 (pp. 162–163).
- Lederer, S. M. 2000. *The Chemical and Physical Properties of the OH, CN, and C₂ Jets in Comet Hale-Bopp (1995 O1)*. Ph.D. thesis, University of Florida.
- Lederer, S. M., H. Campins, and C. M. Lisse 2000. Analysis of OH, CN, and C₂ gas jets in Comet Hale-Bopp through Monte Carlo modeling. *BAAS* **32**(3), 1080–1081.
- Lovell, A. J., F. P. Schloerb, E. A. Bergin, J. E. Dickens, C. H. Devries, M. C. Senay, and W. M. Irvine 1998. HCO⁺ Imaging of Comet C/Hale-Bopp 1995 O1. *Astrophys. J. Lett.* **497**, L117.
- Lovell, A. J., N. Kallivayalil, F. P. Schloerb, M. R. Combi, K. C. Hansen, and T. I. Gombosi 2000. Collisional excitation of HCN by electrons in Comets Hyakutake and Hale-Bopp. *BAAS* **32**(3), 1081.
- Magee-Sauer, K., M. J. Mumma, M. A. DiSanti, N. Dello Russo, and T. W. Rettig 1999. Infrared spectroscopy of the ν_3 band of hydrogen cyanide in Comet C/1995 O1 Hale-Bopp. *Icarus* **142**, 498–508.
- McLean, I. S., E. E. Becklin, O. Bendiksen, G. Brims, J. Canfield, D. F. Figer, J. R. Graham, J. Hare, F. Lacayanga, J. Larkin, S. B. Larson, N. Levenson, N. Magnone, H. Teplitz and W. Wong 1998. The Design and Development of NIRSPEC: A near-infrared Echelle spectrograph for the Keck II telescope. In *Infrared Detector Arrays for Astronomy* (A. M. Fowler, Ed.), pp. 566–578. SPIE Conf. Proc. 3354.
- McLean, I. S. 2000. Scientific results with NIRSPEC on the Keck II Telescope. In *Discoveries and Research Prospects from 8- to 10-Meter-Class Telescopes* (J. Bergeron, Ed.), pp. 203–211. SPIE Conf. Proc. 4005.
- Meier, R., P. Eberhardt, D. Krankowsky, and R. R. Hodges 1993. The extended formaldehyde source in comet P/Halley. *Astron. Astrophys.* **277**, 677–690.
- Mitchell, D. L. et al. 1987. Evidence for chain molecules enriched in carbon, hydrogen, and oxygen in comet Halley. *Science* **237**, 626–628.
- Mitchell, D. L., R. P. Lin, K. A. Anderson, C. W. Carlson, D. W. Curtis, A. Korth, H. Reme, J. A. Sauvaud, C. d'Uston, and D. A. Mendis 1989. Complex organic ions in the atmosphere of comet Halley. *Adv. Space Res.* **9**, 35–39.
- Mumma, M. J., H. A. Weaver, H. P. Larson, D. S. Davis, and M. Williams 1986. Detection of water vapor in Halley's comet. *Science* **232**, 1523–1528.
- Mumma, M. J., P. R. Weissman, and S. A. Stern 1993. Comets and the origin of the solar system: reading the Rosetta stone. In *Protostars and Planets. III* (E. H. Levy and J. I. Lunine, Eds.), pp. 1177–1252, Univ. of Arizona Press, Tucson.
- Mumma, M. J., M. A. DiSanti, N. Dello Russo, M. Fomenkova, K. Magee-Sauer, C. D. Kaminski, and D. X. Xie 1996. Detection of abundant ethane and methane, along with carbon monoxide and water, in Comet C/1996 B2 Hyakutake: Evidence for interstellar origin. *Science* **272**, 1310–1314.
- Mumma, M. J., I. S. McLean, M. A. DiSanti, J. E. Larkin, N. Dello Russo, K. Magee-Sauer, E. E. Becklin, T. Bida, F. Chaffee, A. R. Conrad, D. F. Figer, A. M. Gilbert, J. R. Graham, N. A. Levenson, R. E. Novak, D. C. Reuter, H. I. Teplitz, M. K. Wilcox, and Li-Hong Xu 2001. A survey of organic volatile species in comet C/1999 H1 (Lee) using NIRSPEC at the Keck Observatory. *Astrophys. J.* **546**, 1183–1193.
- Pugh, L. A., and K. Narahari Rao 1976. Intensities from infrared spectra. In *Molecular Spectroscopy: Modern Research* (K. Narahari Rao, Ed.), Vol. 2, pp. 165–227. Academic Press, New York.
- Rank, D. M., C. H. Townes, and W. J. Welch 1971. Interstellar molecules and dense clouds. *Science* **174**, 1083–1101.
- Rodgers, S. D., and S. B. Charnley 1998. HNC and HCN in comets. *Astrophys. J. Lett.* **501**, L227–L230.
- Rothman, L. S., and 13 colleagues 1992. The HITRAN molecular database: editions of 1991 and 1992. *J. Quant. Spectrosc. Radiat. Trans.* **48**, 469–507.
- Sandford, S. A., and L. J. Allamandola 1988. The condensation and vaporization behavior of H₂O:CO ices and implications for interstellar grains and cometary activity. *Icarus* **76**, 201–224.
- Senay, M. S., and D. Jewitt 1994. Coma formation driven by carbon-monoxide release from comet Schwassmann-Wachmann 1. *Nature* **371**, 229–231.
- Snyder, L. E., Palmer, P., and de Pater, I. 1989. Radio detection of formaldehyde emission from Comet Halley. *Astron. J.* **97**, 246–253.
- Tielens, A. G. G. M., A. T. Tokunaga, R. R. Geballe, and F. Baas 1991. Interstellar solid CO-Polar and nonpolar interstellar ices. *Astrophys. J.* **381**, 181–199.
- Tokunaga, A. T., D. W. Toomey, J. Carr, D. N. Hall, and H. W. Epps 1990. Design for a 1-5 micron cryogenic echelle spectrograph for the NASA IRTF. *Proc. Spie* **1235**, 131–143.
- Turner, B.E. 1989. Recent progress in astrochemistry. *Space Sci. Rev.* **51**, 235–337.
- Weaver, H. A., and M. J. Mumma 1984. Infrared molecular emissions from comets. *Astrophys. J.* **276**, 282–297.
- Weaver, H. A., M. J. Mumma, H. P. Larson, and D. S. Davis 1986. Post-perihelion observations of water in Comet Halley. *Nature* **324**, 441–444.
- Weaver, H. A., P. D. Feldman, M. F. A'Hearn, C. Arpigny, J. C. Brandt, and C. E. Randall 1996. *IAU Circ.* 6374.

- Weaver, H. A., T. Y. Brooke, G. Chin, S. J. Kim, D. Bockelée-Morvan, and J. K. Davies 1999. Infrared spectroscopy of comet Hale-Bopp. *Earth, Moon, Planets* **78**, 71–80.
- Whittet, D. C. B., W. A. Schutte, A. G. G. M. Tielens, A. C. A. Boogert, Th. De Graauw, P. Ehrenfreund, P. A. Gerakines, F. P. Helmich, T. Prusti, and E. F. van Dishoeck 1996. An ISO view of interstellar ices: first results. *Astron Astrophys.* **315**, L357–L360.
- Wink, J., D. Bockelée-Morvan, D. Despois, P. Colom, N. Biver, J. Crovisier, E. Gérard, E. Lellouch, J. K. Davies, W. R. F. Dent, and L. Jorda 1999. Evidences for extended sources and temporal modulations in molecular observations of C/1995 O1 (Hale-Bopp) at the IRAM interferometer. *Earth, Moon, Planets* **78**, 63.
- Womack, M., S. A. Stern, and M. C. Festou 1997a. Millimeter-wavelength spectroscopy of CO, HCN, H₂CO, and CH₃OH in C/1996 B2 (Hyakutake). *Planet. Space Sci.* **45**, 711–715.
- Womack, M., M. C. Festou, and S. A. Stern 1997b. The heliocentric evolution of key species in the distantly-active comet C/1995 O1 (Hale-Bopp). *Astron. J.* **114**, 2789–2795.
- Womack, M., M. C. Festou, and S. A. Stern 1999. The detection of carbon monoxide gas emission in (2060) Chiron. *Astronomicheskii Vestnik* **33**, 187–195.
- Womack, M., D. A. Pinnick, J. G. Mangum, M. C. Festou, and S. A. Stern 2000. OTF images of Comet Hale-Bopp. In imaging at radio through submillimeter wavelengths (J. Mangum, Ed.), *Publ. Astron. Soc. Pac. Conf. Series*, p. 75.
- Wooden, D. H., D. E. Harker, C. E. Woodward, H. M. Butner, C. Koike, F. C. Witteborn, and C. W. McMurtry 1999. Silicate mineralogy of the dust in the inner coma of comet C/1995 O1 (Hale-Bopp) pre- and post-perihelion. *Astrophys. J.* **517**, 1034–1058.
- Xie, X., and M. J. Mumma 1992. The effect of electron collisions on rotational populations of cometary water. *Astrophys. J.* **386**, 720–728.
- Xie, X., and M. J. Mumma 1996a. Monte Carlo simulation of cometary Atmospheres: Application to Comet P/Halley at the time of the Giotto Spacecraft encounter. I. Isotropic model. *Astrophys. J.* **464**, 442–456.
- Xie, X., and M. J. Mumma 1996b. Monte Carlo simulation of cometary Atmospheres: Application to Comet P/Halley at the time of the Giotto Spacecraft encounter. II. Axisymmetric model. *Astrophys. J.* **464**, 457–475.
- Yamamoto, T. 1982. Evaluation of infrared line emission from constituent molecules of cometary nuclei. *Astron. Astrophys.* **109**, 326–330.